Article

SOURCE DATA | TRANSPARENT PROCESS | OPEN ACCESS

THE EMBO JOURNAL

TFG binds LC3C to regulate ULK1 localization and autophagosome formation

Marianna Carinci[1,2], Beatrice Testa[3], Matteo Bordi[1,3], Giacomo Milletti[1,3], Massimo Bonora[2], Laura Antonucci[1], Caterina Ferraina[1], Marta Carro[4], Mukesh Kumar[5], Donatella Ceglie[1], Franziska Eck[6], Roberta Nardacci[7], Francois le Guerroué[6], Stefania Petrini[8], Maria E Soriano[4], Ignazio Caruana[1], Valentina Doria[8], Maria Manifava[9], Camille Peron[10], Matteo Lambrughi[5], Valeria Tiranti[10], Christian Behrends[6], Elena Papaleo[5,11], Paolo Pinton[2], Carlotta Giorgi[2], Nicholas T Ktistakis[9], Franco Locatelli[1,12], Francesca Nazio[1,*,†] & Francesco Cecconi[1,3,13,**,†]

Abstract

The early secretory pathway and autophagy are two essential and evolutionarily conserved endomembrane processes that are finely interlinked. Although growing evidence suggests that intracellular trafficking is important for autophagosome biogenesis, the molecular regulatory network involved is still not fully defined. In this study, we demonstrate a crucial effect of the COPII vesicle-related protein TFG (Trk-fused gene) on ULK1 puncta number and localization during autophagy induction. This, in turn, affects formation of the isolation membrane, as well as the correct dynamics of association between LC3B and early ATG proteins, leading to the proper formation of both omegasomes and autophagosomes. Consistently, fibroblasts derived from a hereditary spastic paraparesis (HSP) patient carrying mutated TFG (R106C) show defects in both autophagy and ULK1 puncta accumulation. In addition, we demonstrate that TFG activity in autophagy depends on its interaction with the ATG8 protein LC3C through a canonical LIR motif, thereby favouring LC3C-ULK1 binding. Altogether, our results uncover a link between TFG and autophagy and identify TFG as a molecular scaffold linking the early secretion pathway to autophagy.

Keywords autophagy; ERGIC; LC3C; TFG

Subject Categories Autophagy & Cell Death; Membranes & Trafficking
DOI 10.15252/embj.2019103563 | Received 26 September 2019 | Revised 17 February 2021 | Accepted 1 March 2021 | Published online 1 May 2021
The EMBO Journal (2021) 40: e103563

Introduction

Macroautophagy (hereafter autophagy) is an evolutionarily conserved catabolic process, by which double-membrane vesicles deliver intracellular macromolecules and organelles to lysosomes for degradation. Upon induction of autophagy by different stimuli, autophagosomes form *de novo* and initially appear as small membrane structures referred to as isolation membrane (IM) or phagophores. IM expands, gradually engulfing portions of the cytoplasm, and gives rise to autophagosomes. The formation of an autophagosome requires the action of autophagy-related (ATG) proteins that are organized into functional complexes (Mizushima *et al,* 2011), which localize to the IM at some stage of autophagosome formation. The Unc-51-like kinase 1 (ULK1) complex and the [(phosphatidylinositol (3)] kinase complex III (PIK3C3), together with the activation of localized phosphatidylinositol (PI) synthase (Nishimura *et al,* 2017), lead to the production of PI3P, which acts as a platform for the recruitment of effector proteins, including the double FYVE domain-containing factor DFCP1 (Axe *et al,*

1 Department of Pediatric Hemato-Oncology and Cell and Gene Therapy, IRCCS Bambino Gesù Children's Hospital, Rome, Italy
2 Department of Medical Sciences, University of Ferrara, Laboratory of Technologies for Advanced Therapy (LTTA), Technopole of Ferrara, Ferrara, Italy
3 Department of Biology, University of Rome Tor Vergata, Rome, Italy
4 Department of Biology, University of Padua, Padua, Italy
5 Computational Biology Laboratory, Danish Cancer Society Research Center, Copenhagen, Denmark
6 Munich Cluster for Systems Neurology (SyNergy), Ludwig-Maximilians-Universität (LMU), München, Germany
7 Department of Epidemiology and Preclinical Research, National Institute for Infectious Diseases IRCCS "L. Spallanzani", Rome, Italy
8 Confocal Microscopy Core Facility, Research Laboratories, IRCCS Bambino Gesù Children's Hospital, Rome, Italy
9 The Babraham Institute, Cambridge, UK
10 UO Medical Genetics and Neurogenetics, Fondazione IRCCS Istituto Neurologico C. Besta, Milan, Italy
11 Translational Disease Systems Biology, Faculty of Health and Medical Sciences, Novo Nordisk Foundation Center for Protein Research University of Copenhagen, Copenhagen, Denmark
12 Department of Gynecology/Obstetrics and Pediatrics, Sapienza University, Rome, Italy
13 Unit of Cell Stress and Survival, Danish Cancer Society Research Center, Copenhagen, Denmark
*Corresponding author. Tel: +39 06 68592895; E-mail: francesca.nazio@opbg.net
**Corresponding author. Tel: +45 3 5257302; E-mail: cecconi@cancer.dk
†These authors contributed equally to this work

© 2021 The Authors. Published under the terms of the CC BY NC ND 4.0 license

2008) and WIPI proteins (Funderburk *et al,* 2010). This phase is followed by the recruitment of the remaining autophagy core machinery involved in phagophore expansion, including ATG9, and two ubiquitin-like conjugation systems, ATG12 ~ ATG5 and ATG16L1 (Mizushima *et al*, 2003). These complexes process small ATG8 ubiquitin-like proteins [microtubule-associated protein 1A/1B-light chain 3 (LC3) and GABARAP family members)] (Slobodkin & Elazar, 2013), to membrane-associated PE. LC3 incorporation represents the maturation step of autophagosomes, which in the end fuse with lysosomes, where their content is digested by lysosomal hydrolases and released into the cytosol for recycling.

Over the years, a strict connection between autophagy and vesicular transport processes is emerging. In particular, the coat protein complex II (COPII), the first component involved in the transport pathway that leads out of the cell, has been linked to autophagosome formation. COPII transport carriers are composed of two distinct layers: an inner coat characterized by SEC23/SEC24 and an outer coat formed by SEC13/SEC31. They originate at the ER exit sites (ERES) and are essential for cellular cargo transport to the ER-Golgi intermediate compartment (ERGIC). ERES, ERGIC and COPII vesicles have been shown to co-localize with sites of autophagosome biogenesis (Karanasios *et al,* 2016; Stadel *et al,* 2015; Ge *et al,* 2013; Ge *et al*, 2014; Jeong *et al,* 2018), whereas a number of proteins involved in this early secretory pathway are found to directly contribute to autophagy regulation (Moyer *et al,* 2001; Zoppino *et al,* 2010). Indeed, in both yeast (sec12, sec16, sec23, sec24) (Ishihara *et al,* 2001; Davis *et al,* 2016) and mammals (SEC23A) (Ge *et al*, 2014), deficiency of SEC proteins was found to impair autophagy (Ishihara *et al,* 2001). Furthermore, COPII components physically interact with core proteins required for autophagy (Lord *et al,* 2011; Wang *et al,* 2014; Davis *et al,* 2016; Gan *et al,* 2017). However, how the *regulators* of COPII vesicle transport are controlled in response to nutrient deprivation, and to allow their impact to autophagosome formation, is largely unknown.

TFG (TRK-fused gene) is a SEC16-interacting protein ubiquitously expressed in human cells (Witte *et al,* 2011). TFG appears to coordinate the distribution of COPII transport carriers, promoting their uncoating < and retaining these vesicles at the region between the ER and the ERGIC, in order to facilitate their fusion with the latter compartment (Witte *et al,* 2011; Johnson *et al,* 2015; Hanna *et al,* 2017). In humans, TFG mutations cause sensory axon degeneration, hereditary spastic paraplegia and Charcot–Marie–Tooth disease type 2 (Takashima *et al,* 1997; Beetz *et al,* 2013; Tsai *et al,* 2014). In these neuronal disorders, the defects appear related to structural changes in the ER-associated processes, such as ER architecture maintenance and ER export. Besides these, autophagy impairment is also emerging as a central process in the pathogenesis of such complicated forms of neuropathy (Colecchia *et al,* 2018).

Although very recently, and in a specific immune system model, a link between TFG and autophagy has been found (Steinmetz *et al,* 2020), no details are known about the molecular mechanisms of this interplay and its control. In the present study, we identify the mechanisms of TFG–autophagy interplay. By using a combination of biochemical, morphological and functional analyses, we clearly demonstrate the interaction between TFG and the autophagy kinase ULK1 and, in particular, the crucial role of TFG in ULK1 proper localization during nutrient deprivation. Moreover, TFG-deficient cells exhibit decreased LC3B-II levels and a delay in the association of LC3B to the isolation membrane components, defining a primary role for TFG in autophagosome formation. Consistently, fibroblasts derived from a HSP patient carrying mutated TFG (R106C) show defects in both autophagy and ULK1 puncta accumulation. Last, our report reveals that, *via* a canonical LC3-interacting region (LIR) motif, TFG interacts with LC3C; hence, this binding is required for regulating the proper distribution of ULK1 and the formation of autophagosomes. This implies the need for a LIR-dependent TFG-LC3C interaction as a positive regulatory step in autophagosome formation.

Results

TFG interacts with ULK1 and regulates its stability and localization, independently of the COPII pathway

By an unbiased proteomics-based approach to identify ULK1-interacting proteins, performed in a previous study (Nazio *et al,* 2016), we identified TFG as a putative ULK1-interacting protein. The recent discovery of a link between COPII and autophagy (Ge *et al*, 2014; Jeong *et al,* 2018) and the fact that TFG is known to be involved in facilitating COPII vesicle export (Johnson *et al,* 2015) and to prime autophagy in specific experimental immune system models (Steinmetz, *et al,* 2020) prompted us to investigate the mechanisms of TFG-ULK1 interaction in autophagy regulation. First, to characterize the interaction at endogenous levels, we isolated endogenous TFG by co-immunoprecipitation and analysed ULK1-complex members (ULK1, ATG13 and FIP200). Each member analysed shows interaction with TFG (Fig 1A), as also confirmed by immunofluorescence (IF): further, we detected a tight association between TFG, ULK1 and ATG13 during autophagy induction by starvation (Figs 1B and EV1A). Second, to investigate the functional significance of the TFG-ULK1 interaction, we examined the effects of TFG depletion on both ULK1 protein levels and activity. Since long periods of TFG depletion result in an inhibition of cellular proliferation and in an increase in cell death (Johnson *et al,* 2015), we chose the 48–60 h timepoint of siRNA treatment for all subsequent experiments. In Fig 1C-E, we observed, in TFG-silenced cells, an increase in the steady-state levels of ULK1, but no changes in the phosphorylation levels of ULK1 substrates ATG13 and ATG14 (Fig EV1B). Of note, such an effect on protein stability is specific for ULK1, since TFG depletion does not impact at all ATG13 and FIP200 levels (Fig EV1C).

Third, since once activated, the ULK1 complex translocates to puncta to prime autophagosome biogenesis (Karanasios *et al,* 2013), we assessed whether TFG could influence ULK1 puncta formation and, to this aim, measured ULK1 puncta number after TFG downregulation. Indeed, there is a significant increase in ULK1 puncta number in fed conditions, and this effect is exacerbated during autophagy induction by starvation (Figs 1F and EV1D). Also, since ATG13 puncta may often recapitulate ULK1 puncta localization during starvation (Karanasios *et al,* 2013 and Fig EV1E), we evaluated whether or not TFG also affected ATG13 puncta formation in our system. As shown in Figs 1G and EV1F, ATG13 puncta also increase in TFG-depleted cells with a significant spread upon starvation, and TFG overexpression is able *per se* to rescue this phenotype.

Last, since it is well established that TFG has a direct role in COPII vesicle localization (Johnson *et al,* 2015), we decided to

 © 2021 The Authors

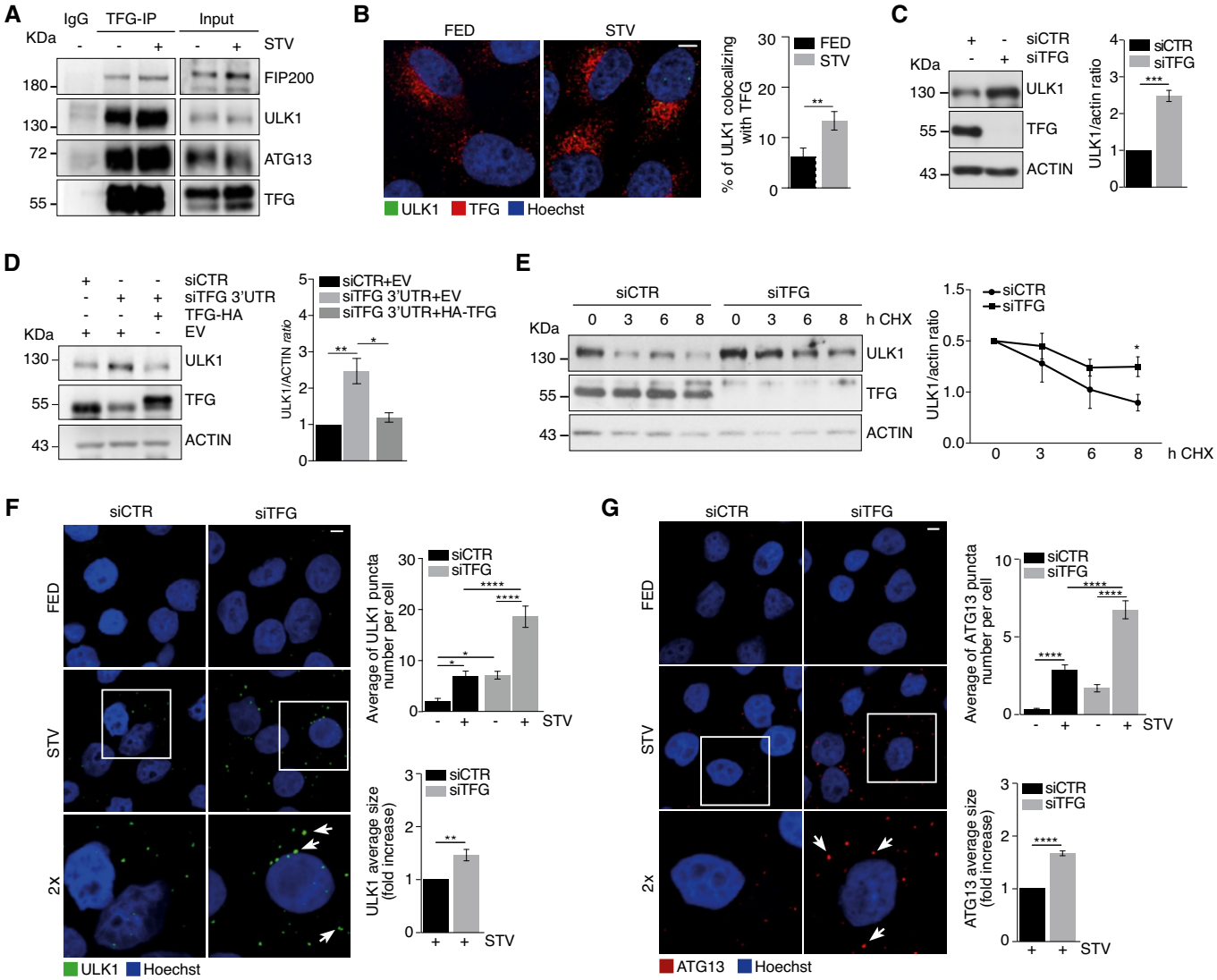

Figure 1. TFG interacts with ULK1 and regulates its stability and localization.

A HeLa cells were cultured in complete growth or starvation (STV) media for 30'. Cell lysates were immunoprecipitated (IP) with anti-TFG antibody or IgG as a negative control. Immunoprecipitated complexes were analysed by WB to detect TFG, ULK1, ATG13 and FIP200 as indicated.

B HeLa cells were cultured in complete growth (FED) or starvation (STV) media for 1 h. Cells were fixed, permeabilized and labelled with anti-TFG (red) and anti-ULK1 (green) antibodies, respectively. Hoechst was used to stain nuclei. Co-localization analysis was performed by ImageJ plugin Jacop and reported in the graph (right). Values of Mander's coefficient for ULK1 are expressed as mean ± SEM. Significance was assigned by unpaired Student's *t*-test. $^{**}P < 0.01$ ($n = 3$ independent experiments, $n = 12$ fields analysed). Scale bar 5 μm.

C HeLa cells were transfected with specific RNAi oligonucleotides (siTFG) or unrelated oligonucleotides as a negative control (siCTR) for 48 h. Protein extracts were analysed by WB to detect ULK1, TFG and ACTIN as indicated. Densitometry analysis of ULK1 over ACTIN is shown (right). All values are mean ± SEM. Statistical analyses were performed by two-tailed Student's *t*-test. $^{***}P < 0.001$ ($n = 3$ independent experiments).

D HeLa cells were co-transfected with control siRNA and an empty vector (EV), or 3'UTR TFG siRNA together with an EV or HA-TFG plasmids. Protein extracts were analysed by WB to detect ULK1, TFG and ACTIN as indicated. Densitometry analysis of ULK1 protein levels normalized over ACTIN is also reported (right). All values are expressed as the mean ± SEM. Statistical analyses were performed by one-way ANOVA followed by Tukey's multiple comparison test. $^{*}P < 0.05$ and $^{**}P < 0.01$ ($n = 3$ independent experiments).

E HeLa cells were transfected as in C), grown in the presence or not of cycloheximide (CHX) for indicated time periods. Protein extracts were analysed by WB to detect ULK1, TFG and ACTIN as indicated. Densitometry analysis of ULK1 normalized over ACTIN is also shown (right). Values are mean ± SEM Statistical analyses were performed by multiple *t*-test. $^{*}P < 0.05$ ($n = 3$ independent experiments).

F, G HeLa cells were treated as in B) and then fixed and stained with ULK1 (green) (F) or ATG13 (red) antibodies (G), respectively. Hoechst was used to stain nuclei. Graphs (right) show the average of both ULK1 (F) ($n = 3$ independent experiments, $n = 11$ fields analysed) and ATG13 ($n = 3$ independent experiments, $n \geq 16$ fields analysed) (G) puncta number per cell and both ULK1 ($n = 3$ independent experiments) (F) and ATG13 ($n = 3$ independent experiments) (G) fold of increase of the average size, respectively. White arrows indicate most representative puncta of analysed conditions. All data are reported as the mean value ± SEM. Statistical analyses were performed by two-way ANOVA followed by Tukey's multiple comparison test. $^{*}P < 0.05$ and $^{****}P < 0.0001$ or by unpaired Student's *t*-test when two groups were compared. $^{**}P < 0.01$ and $^{****}P < 0.0001$. Scale bar 5 μm.

Source data are available online for this figure.

© 2021 The Authors

investigate whether TFG-dependent effect on ULK1 could be related to TFG role in the COPII pathway. To this aim, we analysed ULK1 puncta number formation upon depletion of both SEC23A and SEC16, two important components of the COPII pathway. As shown in Fig EV1G and H, there are no significant differences in ULK1 puncta number in the conditions analysed, when compared to the control. To support this result, we analysed ULK1 protein levels in both SEC23A- and SEC16-depleted cells, respectively, and found no relevant changes when compared to TFG-depleted cells, at variance with the effect of SEC23A downregulation on autophagy flux (Fig EV1I-J) (Ge *et al*, 2014). In order to exclude that such an effect of TFG on ULK1 could be a consequence of TFG deficiency on COPII vesicles, we analysed both ULK1 puncta formation and protein levels after TFG-SEC23A or TFG-SEC16 depletion. As shown in Fig EV1K and L, ULK1 puncta number and protein levels are still increased in both conditions analysed, indicating that the increment of ULK1 does not depend on the presence of COPII vesicles.

Altogether, these results show that TFG i) controls ULK1 protein levels at a steady state, ii) regulates ULK1-ATG13 puncta number and size, and iii) acts on ULK1 puncta formation independently of its function in the COPII pathway.

TFG is essential for proper ULK1 complex distribution during autophagy

Based on these data, we set up experiments in order to verify ULK1 puncta distribution upon TFG depletion. To this aim, we evaluated ULK1 puncta co-localization by IF with several intracellular structures: ER, ATG9-positive vesicles, Golgi complex, COPII vesicles and ERGIC, respectively. In control conditions, upon autophagy induction, there is an increase in ULK1 puncta that co-localize with both ER and ATG9 (Figs 2A and EV2A); this increase does not occur when TFG is depleted and autophagy is induced. About ULK1–Golgi complex association, we observed no differences in all conditions analysed (Fig 2B). Of note, the ERGIC compartment has been proposed as an important membrane source for autophagosome formation, and it was suggested that upon autophagy induction, ERGIC-derived COPII vesicles act as template for LC3 lipidation (Ge *et al*, 2014). Therefore, we investigated whether TFG depletion could affect or not ULK1 puncta localization to both COPII vesicles and ERGIC compartments, by analysing the percentage of ULK1 puncta co-localizing with SEC31A and ERGIC53, respectively. Strikingly, while TFG depletion upon autophagy induction does not induce significant variation in the association between ULK1 and COPII (Fig 2C), the percentage of ULK1 puncta juxtaposed to the ERGIC structures significantly increased in the same condition (Fig 2D). Moreover, we evaluated the association between ULK1-ERGIC upon TFG depletion and autophagy induction through a super-resolution analysis by structured illumination microscopy (SIM). As shown in Fig 2E, we found that, upon TFG downregulation, a portion of ULK1 puncta is ERGIC-associated, with this defining TFG as an important factor for a close juxtaposition between ULK1 and ERGIC. Indeed, we also succeeded to restore canonical ULK1-ERGIC co-localization by simply re-expressing TFG in a classical rescue experiment (Fig 2F).

In sum, this set of results highlights a role for TFG in controlling ULK1 puncta subcellular distribution during autophagy induction.

Inhibition of TFG results in impaired autophagy flux as a consequence of stalled omegasomes

In order to evaluate whether or not TFG knockdown had an impact on the autophagy flux, we analysed the LC3B status by different approaches. First, a significant reduction in the number of LC3B puncta, which measure *early* LC3B-II recruitment to autophagosomes (Itakura & Mizushima, 2010), is visible only upon starvation (+STV/+CLQ), when comparing control with TFG-depleted cells (Fig 3A). Second, Western Blot (WB) analyses reveal a significant decrease in LC3B-II protein levels after both starvation and TFG depletion, in the presence of CLQ, when compared with controls (Fig EV3A). Third, the co-localization between LC3B-II puncta and LAMP1, an endosomal and lysosomal marker, shows that TFG depletion impacts on autophagosome clearance, when compared with control cells (Fig 3B). Altogether, these results support the concept of a global impairment of the autophagy process after TFG depletion.

Next, given the impact of TFG on the ULK1 complex, we decided to evaluate whether loss of TFG also affected the number and size of other *early* autophagy proteins: ATG16L1, a FIP200-interacting protein (Gammoh *et al,* 2013; Nishimura *et al,* 2013), belonging to the ATG12–5/16 complex, and DFCP1, a marker of omegasomes (Karanasios *et al,* 2013). As shown in Fig 3C, we found a significant increase in ATG16L1 puncta formation after TFG downregulation upon starvation. Omegasome structures were then analysed by using an HEK293 cell line stably expressing green fluorescence protein (GFP)-DFCP1 (Axe *et al,* 2008). Interestingly, DFCP1-labelled structures are significantly increased in both number and size upon TFG depletion, as shown in Fig 3D. Our data thus suggest that depletion of TFG causes a significant increase of early pro-autophagy complexes, most likely by inducing omegasome stalling. This is due to the effect of TFG on ULK1 since, as shown in Fig EV3B, the increment of ATG16L1 puncta is overturned by ULK1 depletion.

Further, we evaluated the association and the dynamics between IM components (ULK1 complex, DFCP1) and LC3B, since DFCP1 marks a transient omegasome, whereas LC3B is recruited shortly after DFCP1 at the omegasome and becomes then trapped on the inner membrane of a complete autophagosome until its degradation. Thus, we proved that starvation is able to promote a significant reduction in endogenous ULK1-LC3B association after TFG depletion in HeLa cells (Fig 4A). Moreover, by a co-IP assay, we found a decrease in ULK1-LC3B-II interaction in the same conditions (Fig EV4A). Next, we overexpressed ATG13, a reliable marker (and less cytotoxic than ULK1 itself) of the ULK1 complex, and DFCP1, as a marker of the omegasome, to examine in depth the dynamics of their association with LC3B by means of a live imaging-based approach. To this aim, we employed HEK293 cells stably expressing GFP-ATG13 or GFP-DFCP1, respectively, in which we co-transfected a plasmid encoding for cyan fluorescence protein (CFP)-LC3B, in the presence or absence of TFG. In Fig 4B-C (and Fig EV4B-C; Movies EV1-EV4) is shown that, upon TFG downregulation, the lifespan of both ATG13 (340 s vs. 200 s in control conditions) and DFCP1 (580 s vs. 400 s in control conditions) is significantly extended. Also, in the same condition, i.e. upon TFG depletion, the appearance of LC3B on ATG13 particles (70 s vs. 40 s in control conditions) or DFCP1 structures (140 s vs. 90 s in control conditions) shows a significant delay. In sum, these results indicate that depletion of TFG perturbs the correct dynamic relationships between pro-autophagic proteins.

 © 2021 The Authors

Next, to monitor at an ultrastructural level the appearance of disturbed autophagosomes in TFG-depleted conditions, we performed a detailed transmission electron microscopy (TEM) analysis (Fig 4D). Indeed, upon TFG depletion and autophagy induction, we observed the occurrence of what we termed "Abnormal structures" (As), containing multiple smaller compartments, multilamellar structures and single-membrane vesicles including electron-dense intraluminal material; by contrast, in control starved cells no significant accumulation of waste materials, a sign of proper execution of autophagy, was detectable. Indeed, a cytosolic accumulation of such As is compatible with an impairment of autophagy, and these structures were in fact positive for ATG13, ATG16L and RAB7, as shown by correlative EM (CLEM) experiments (Fig 4E).

Of the highest interest in biomedicine, mutations within the TFG coiled-coil domain (amino acids 97–124) have been proposed to impair its function and underlie early-onset forms of HSP (Beetz

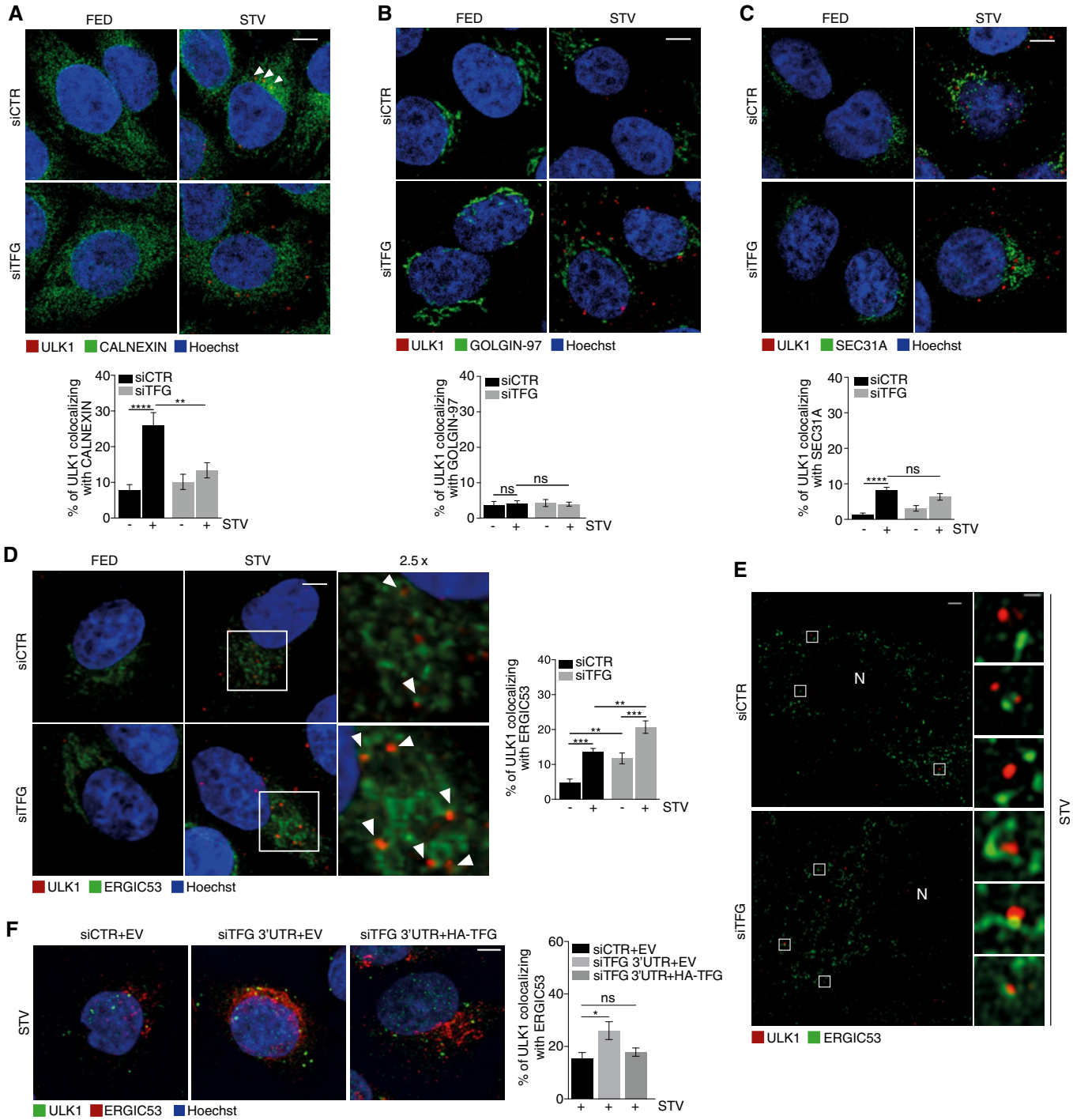

Figure 2.

Figure 2. TFG is essential for proper ULK1 complex distribution during autophagy.

A–D HeLa cells were transfected with specific RNAi oligonucleotides (siTFG) or unrelated oligonucleotides as a negative control (siCTR) and grown in fed or starved conditions for 1 h. Cells were fixed and co-labelled with ULK1 (red) antibody and (A) anti-CALNEXIN (green) antibody to highlight ER structures ($n = 3$ independent experiments, $n \geq 16$ fields analysed), (B) GOLGIN-97 (green) antibody to label GOLGI complex ($n = 3$ independent experiments, $n = 12$ fields analysed), (C) SEC31A (green) to point out COPII vesicles ($n = 3$ independent experiments, $n \geq 16$ fields analysed) and (D) ERGIC53 (green) to mark ERGIC compartment ($n = 3$ independent experiments, $n \geq 14$ fields analysed). Analysis of ULK1 localization with each compartment is reported in each graph. Co-localization analyses were performed by ImageJ plugin Jacop. Values of Mander's coefficient for ULK1 are expressed in percentage as mean ± SEM. Statistical analyses were performed by two-way ANOVA followed by Tukey's multiple comparison test. $^{**}P < 0.01$; $^{***}P < 0.001$; $^{****}P < 0.0001$; and ns, not significant. Scale bars 5 μm. White arrowheads point at ULK1 puncta associated with the analysed markers.

E HeLa cells were transfected as in A), labelled with the indicated antibodies and imaged by SIM microscope. Scale bar in large panels, 5 μm; in small panels, 1 μm. N, nucleus.

F HeLa cells were co-transfected with control siRNA and an empty vector (EV), or 3'UTR TFG siRNA together with an EV or HA-TFG plasmids. Cells grown for 1 h in starvation medium then fixed, permeabilized and labelled with anti-ULK1 (green) and anti-ERGIC53 (red) antibodies, respectively. Hoechst was used to stain nuclei. Co-localization analysis was performed as in (D). Values of Mander's coefficient for ULK1, expressed *as* percentage, are mean ± SEM. Statistical analyses were performed by one-way ANOVA followed by Dunnett's multiple comparison test. $^{*}P < 0.05$; ns, not significant ($n = 3$) ($n = 3$ independent experiments, $n \geq 9$ fields analysed). Scale bar 5 μm.

Source data are available online for this figure.

et al, 2013; Harlalka *et al,* 2016). Thus, we tested fibroblasts from a patient with homozygous variant p.R106C in TFG (Catania *et al,* 2018) and observed a reduction in autophagy flux (Figs 4F and EV4D and F), a significant accumulation of ULK1 puncta when compared with controls (Fig 4G), together with a massive presence of As (Fig EV4E). Additionally, decreased autophagy flux was observed by exogenously expressing an HA-TFG^{R106C} mutant construct in HeLa cells (Fig EV4G).

Altogether, these results clearly indicate that TFG is important for a proper autophagy progression and more precisely in the transition phase between autophagosome initiation and elongation. Also, this role may be relevant in HSP.

The role of TFG in autophagy requires its LIR-dependent association with LC3C

Given that TFG is necessary for the recruitment of LC3B to IM components, and since ERGIC/ERES compartments represent a primary membrane source necessary to trigger LC3B lipidation (Ge *et al,* 2013; Ge *et al,* 2014), we investigated TFG interaction with individual members of the LC3 family. First, we performed a GST pulldown assay by using human LC3 isoforms (LC3A, LC3B and LC3C) and found that TFG is able to bind all LC3 members with different strength and with a clear preference for LC3C (Fig 5A). Also, LC3C, at variance with LC3A-B, clearly co-immunoprecipitates with TFG (Fig EV5A). Of note, since most proteins that interact with LC3 members are themselves degraded by autophagy, we induced autophagy by starvation and treated cells with ammonium chloride (NH_4Cl), a well-known lysosome inhibitor, in a time course. As shown in Fig EV5B, no changes in TFG protein levels are detected, suggesting that TFG is not merely an autophagy substrate but may act as a regulatory ATG8-interacting protein. Indeed, ATG8-interacting proteins bind non-covalently both LC3 and GABARAP proteins via a short linear sequence named LIR (Rogov *et al,* 2014). We identified three possible LIR motifs of TFG with similar position-specific scoring matrix (PSSM) (Fig EV5C) located in the regions 31–36 (LIR1), 166–171 (LIR2) and 361–366 (LIR3), respectively. We then analysed their propensity to disorder or their capability to be located in folded protein domains. We thus noticed that the LIR 31–36 is located within a predicted PB1 domain for TFG, a domain also found in another LIR-containing protein, p62, and known to be involved in protein–protein interactions (Kirkham, 1974). The region 166–171, which has the lowest PSSM score, is not predicted to be fully disordered according to the consensus in MobiDB, and it has small propensity for helical structures according to an analysis with FELLS. The LIR in the region 361–366 thus seems, in principle, to be the most suitable candidate due to its localization in a disordered region of the protein with also "anchor" motifs, which are common to LIRs (Jacomin, *et al,* 2016). Moreover, we obtained a model of the TFG PB1 domain (residues 10–91) by using as a template the PB1 domain from protein kinase C (Fig 5B and Table EV1) and used this model to rule out that the LIR residues 31–36 could in fact be accessible for interaction with the LC3s. The two key residues for interaction with the hydrophobic grooves of LC3 proteins, Y33 and L36, featured a solvent accessibility of their side chain atoms of 26 and 6.2%, respectively (Birgisdottir, *et al,* 2013; Johansen & Lamark, 2020). This confirms that the region 31–36, despite containing a sequence similar to a LIR motif, is almost buried in the PB1 domain and not available for interaction with LC3 proteins. Our analyses thus point to LIR3, located in the C-terminal region 361–366 (361-PGFTSL-366), as a *bona fide* functional LIR for interaction between TFG and the LC3s, with 363F and 366L occupying the hydrophobic HP1 and HP2 pockets, respectively. To next verify whether TFG binds human ATG8 proteins in a LIR-dependent manner, we generated two HA-tagged TFG LIR mutant constructs (HA-TFG^{mutLIR2} and HA-TFG^{mutLIR3}). In particular, the aromatic residue phenylalanine (F) at position 1 and the hydrophobic residue leucine (L) at position 4 were changed into alanine (A) in both mutant constructs (Fig EV5D). By GST pulldown assay, we next tested whether each TFG-LIR3 mutant construct was able or not to abrogate the capability of TFG to interact with LC3 and GABARAP family members. As shown in Figs 5C and EV5E, mutations of the LIR3 motif decrease significantly the affinity of TFG for both LC3B and LC3C, but not for LC3A or any GABARAP family members. Taking into consideration that i) LC3C recruits the secretion-autophagy co-regulating protein TECPR2 to ERES (Stadel *et al,* 2015), ii) LC3C is required for recruiting other ATG8 orthologues to the site of autophagosome formation (Von Muhlinen *et al,* 2012), iii) LC3C shows the strongest affinity for TFG and iv) no obvious co-immunoprecipitation of LC3A and LC3B with TFG was detected (Fig EV5A), we analysed more in depth the involvement of LIR3 in the TFG-LC3C binding. First, we confirmed the expression of endogenous LC3C in HeLa cells, by

 © 2021 The Authors

analysing its mRNA levels (Fig EV5F); next, we took advantage from a HeLa cell line harbouring endogenously expressed HA-tagged LC3C. As shown in Fig 5D, we confirmed by co-IP that the LC3C-TFG interaction is dramatically decreased in the presence of $TFG^{mutLIR3}$, at variance with HA-$TFG^{mutLIR2}$ (Fig EV5G and H).

Next, to assess the functional importance of the TFG-LC3C interaction in autophagy, we evaluated the autophagy flux after complementing TFG-deficient cells with TFG^{wtLIR} or $TFG^{mutLIR3}$, respectively. As shown in Fig 5E, LC3B-II levels are reduced by the TFG mutant construct, when compared with the WT form. Consistent with this observation, ULK1 canonical protein levels are recovered upon complementation with TFG^{wtLIR} but not with $TFG^{mutLIR3}$ (Fig 5F). Next, we performed an IF analysis to test the importance of TFG-LC3C interaction in both ULK1 puncta formation and intracellular localization. As shown in Fig 5G and H, the integrity of the LIR motif is critical for both formation and distribution of ULK1 complex puncta. Indeed, in live imaging experiments, by analysing co-tracking percentage of ATG13 puncta with both ERES/ERGIC (labelled by SEC16, Figs 5I and EV5I) and TFG^{wtLIR} or $TFG^{mutLIR3}$, respectively (Figs 5J and EV5J), we found that the TFG-LC3C interaction is functional to ULK1 complex distribution and to the TFG-ULK1 association. In line with this, we were able

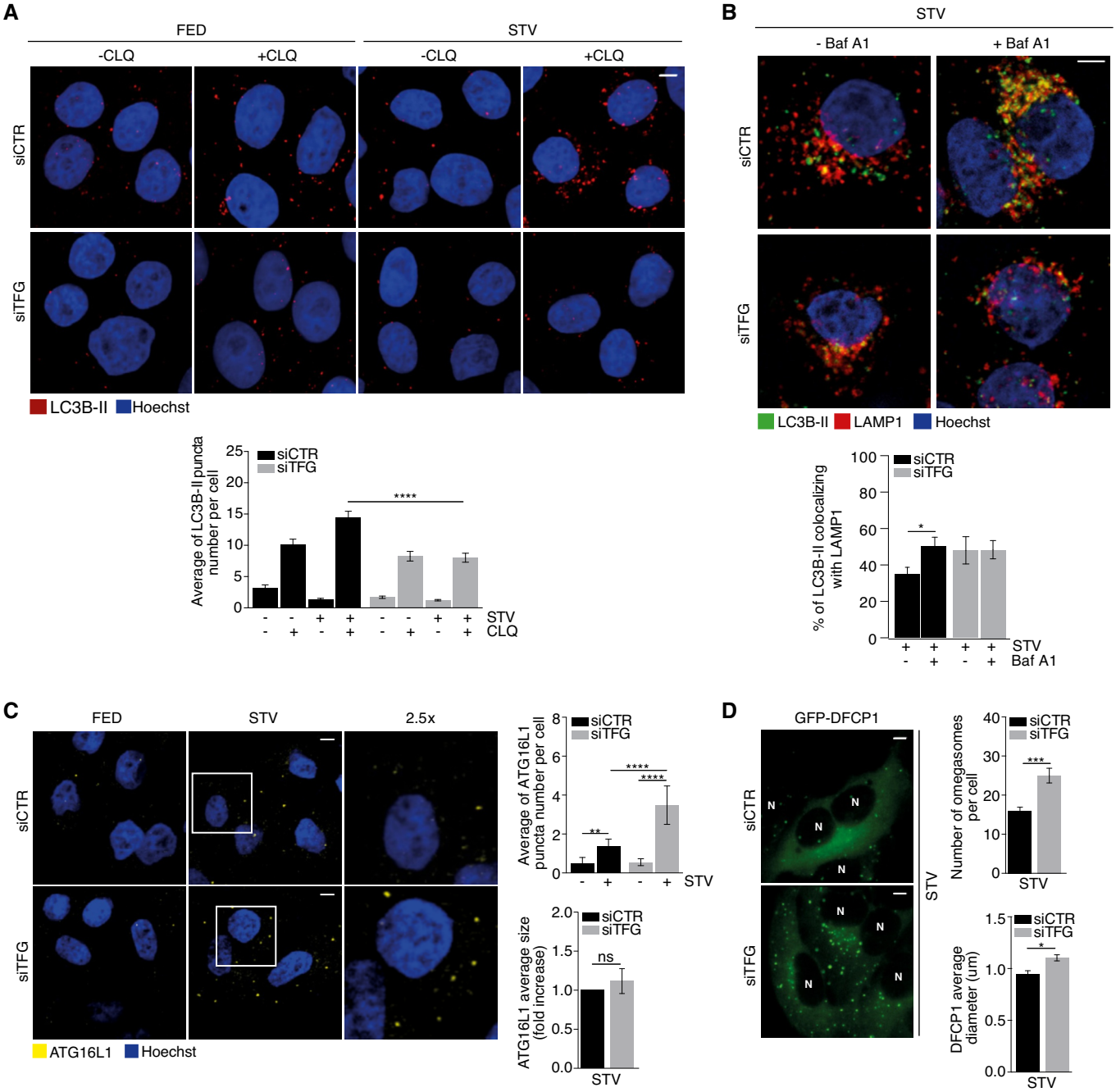

Figure 3.

Figure 3. Inhibition of TFG results in impaired autophagy flux.

A HeLa cells were transfected with specific RNAi oligonucleotides (siTFG) or unrelated oligonucleotides as a negative control (siCTR) and grown in fed (FED) or starvation conditions (STV) in the presence or absence of CLQ for 1 h. Cells were then fixed and stained using LC3B-II (red) antibody. Analysis of LC3B-II puncta number is reported (bottom). All data are expressed as the mean value ± SEM. Statistical analysis were performed by two-way ANOVA followed by Tukey's multiple comparison test. ****$P < 0.0001$ ($n = 4$ independent experiments, $n \geq 25$ fields analysed). Scale bar 5 μm.

B HeLa cells were transfected as in A) and cultured in starvation conditions (STV) in the presence or absence of bafilomycin A1 (Baf A1) for 1 h. Cells were then fixed and stained using LC3B-II (green) and LAMP1 (red) antibodies. Hoechst was used to mark nuclei. Co-localization analyses were performed by ImageJ plugin Jacop. Values of Mander's coefficient for LC3B-II are expressed as mean ± SEM. Statistical analysis were performed by two-way ANOVA followed by Tukey's multiple comparison test. *$P < 0.05$ ($n = 3$ independent experiments, $n \geq 13$ fields analysed). Scale bar 5 μm.

C HeLa cells were transfected as in A) and grown in fed (FED) or starvation conditions (STV) for 1 h. Cells were then fixed and stained using ATG16L1 (yellow) antibody. ATG16L1 puncta number (upper right) and the average size of ATG16L1 as fold increase (bottom right) were reported. All values are expressed as mean ± SEM. Statistical analyses were performed by two-way ANOVA followed by Tukey's multiple comparison test. **$P < 0.01$ and ****$P < 0.0001$ or by unpaired Student's *t*-test when two groups were compared. ns, not significant ($n = 3$ independent experiments, $n \geq 9$ fields analysed). Scale bar 5 μm.

D HEK293 cells stably expressing GFP-DFCP1 were transfected as in A) and cultured in starved conditions for 40'. Cells were visualized with cellSens microscope for live-cell imaging. Pictures show the images taken at the same number of frames for each video. Analyses of the number of DFCP1 structures per cell (upper right) and the mean of omegasomes structures diameter (μm) (bottom right) were reported. N, nucleus. All values are expressed as mean ± SEM. Statistical analyses were performed by unpaired Student's *t*-test. *$P < 0.05$ and ***$P < 0.001$ ($n = 3$ independent experiments). Scale bar 5 μm.

Source data are available online for this figure.

to detect both ULK1 and TFG in complex with LC3C at an endogenous level (Fig EV5K).

Next, we asked whether or not depletion of ATG8 proteins resulted in a similar phenotype as that detected upon $TFG^{mutLIR3}$ expression. Intriguingly, only knockdown of LC3C (Figs 5K and EV5L–O) significantly increases ULK1 protein levels. Importantly, siLC3C is sufficient *per se* to impair the autophagy flux (Fig EV5P).

Finally, since ULK1 function in autophagy depends on its interaction with ATG8 proteins (Alemu *et al,* 2012; Kraft *et al,* 2012; Wirth *et al,* 2019), we investigated whether TFG could favour ULK1-ATG8s interaction. By co-IP experiments, we found that knockdown of TFG strongly decreases ULK1 complex association with both LC3C and GABARAP during starvation (Figs 5L and EV5Q). This function also depends on the TFG LIR motif, since $TFG^{mutLIR3}$ induces a similar effect (Fig 5M).

Altogether, these findings indicate that the TFG-LC3C interaction is crucial for autophagy progression by regulating ULK1 accumulation, ULK1 puncta localization and ULK1-LC3C/GABARAP binding.

Discussion

Emerging evidence highlights the important crosstalk existing between autophagy and the early secretory pathway, thus emphasizing the multitasking role that proteins involved in a specific process could play in the other one, in response to cellular conditions. In recent years, it became quite apparent that COPII vesicles are important for autophagosome biogenesis (Ge *et al*, 2014). At the interface between ER(ES) and ERGIC, TFG promotes uncoating of COPII vesicles after their release from the ER, with this providing a platform that facilitates fusion between these vesicles and the ERGIC compartment (Johnson *et al,* 2015; Hanna *et al,* 2017). In this study, we identified TFG as a positive regulator of autophagosome formation during autophagy induction by nutrient deprivation. Indeed, depletion of TFG leads to several consequences for functional autophagy. First, we found TFG as an ULK1-interacting protein and that its absence promotes higher levels of ULK1, ATG13 and DFCP1 proteins, suggesting a role for this factor in the transition phase between autophagosome initiation and elongation. In line with the increase of early autophagy markers, ULK1 activity is not impaired upon TFG depletion, and it is still able to recruit proteins that may act at the early steps of autophagosome formation. Of the highest importance, here we show that the effect of TFG depletion on ULK1 is not accounted for by the COPII pathway. In fact, under starvation conditions, at variance with depletion of SEC23 and SEC16, the absence of TFG revealed an increase in puncta number and size of ULK1, ATG13 and DFCP1.

It is well known that ULK1 protein levels are finely regulated upon autophagy induction. In particular, ULK1 is targeted by several E3 ubiquitin ligases, such as NEDD4L (Nazio *et al,* 2016) and CUL3-KLHL20 (Liu *et al,* 2016), which lead to ULK1 degradation by the ubiquitin–proteasome system. Interestingly, ultrastructural data show that, at variance with control conditions, the absence of TFG triggers accumulation of abnormal structures (As) containing multiple smaller compartments and membranes that are compatible with immature and aborted autophagosomes. These structures, positive for the autophagosome markers ATG13 and ATG16L, are quite large in size, possibly because they recruit membranes that are not preloaded with mATG8 orthologs, generating as a consequence an expanded isolation membrane that cannot progress into a complete and fully functional autophagosome. Of note, the structures we found by EM analyses are reminiscent of characteristic multilamellar vesicles called MVBs (multivesicular bodies), and they are also labelled by the MVB marker Rab7. However, since TFG has been identified as a potential interactor of some proteins involved in sorting and formation of MVB (Schlundt, *et al,* 2009; Hein, *et al,* 2015), we cannot exclude that the absence of TFG could also have an effect on this pathway.

In addition, loss of TFG reduces the association between LC3B and the IM components, leading to a delay of dissociation of early autophagy proteins from membranes and an impairment in the autophagosome transition phase between initiation and elongation.

Interestingly, by dissecting the molecular details of the TFG role in autophagy, we identified TFG as novel and unexplored LC3C-binding protein. Indeed, our data argue for a direct close interaction between LC3C and TFG, through a canonical LIR motif that we have mapped in a P/Q rich TFG region. At variance with the established importance of LC3B in autophagy, only a few studies have focused on LC3C in terms of its subcellular localization and regulation (Muhlinen *et al,* 2012; Stadel *et al,* 2015; Liu *et al,* 2017; Le

 © 2021 The Authors

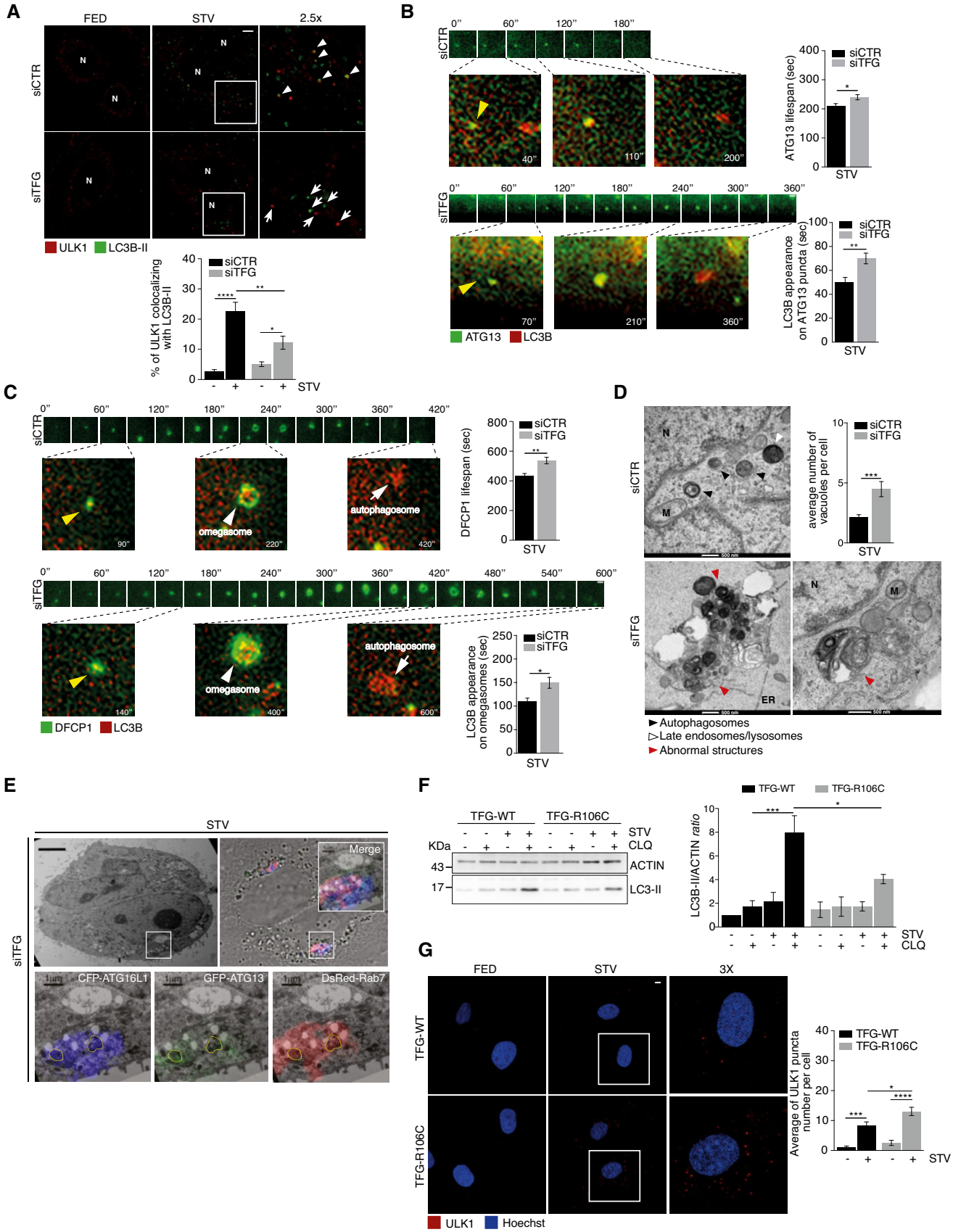
A
FED
STV
2.5x
siCTR
siTFG
N
ULK1
LC3B-II
% of ULK1 colocalizing with LC3B-II
siCTR
siTFG
STV
B
siCTR
siTFG
ATG13 lifespan (sec)
ATG13
LC3B
LC3B appearance on ATG13 puncta (sec)
C
siCTR
siTFG
omegasome
autophagosome
DFCP1 lifespan (sec)
DFCP1
LC3B
LC3B appearance on omegasomes (sec)
D
siCTR
siTFG
average number of vacuoles per cell
N
M
ER
Autophagosomes
Late endosomes/lysosomes
Abnormal structures
E
STV
siTFG
Merge
CFP-ATG16L1
GFP-ATG13
DsRed-Rab7
F
TFG-WT
TFG-R106C
STV
CLQ
KDa
43
17
ACTIN
LC3-II
LC3B-II/ACTIN ratio
G
FED
STV
3X
TFG-WT
TFG-R106C
Average of ULK1 puncta number per cell
ULK1
Hoechst

Figure 4.

Figure 4. Inhibition of TFG results in stalled omegasomes and accumulation of abnormal structures.

A HeLa cells were transfected with specific RNAi oligonucleotides (siTFG) or unrelated oligonucleotides as a negative control (siCTR); after culturing cells in fed (FED) or starvation conditions (STV) for 1 h, cells were fixed and labelled with the indicated antibodies. Co-localization analysis was performed by using ImageJ Jacop plugin and mean ± SEM of Mander's coefficients of ULK1, expressed as percentage, is reported (bottom). White arrowheads point at co-localization events between ULK1 and LC3B-II; white arrows track puncta not co-localizing; N, nucleus. Statistical analyses were performed by two-way ANOVA followed by Tukey's multiple comparison test. $*P < 0.05$; $**P < 0.01$; and $****P < 0.0001$ ($n = 3$ independent experiments, $n \geq 16$ fields analysed). Scale bar 5 μm.

B, C HEK293 cells stably expressing either GFP-ATG13 (B) or GFP-DFCP1 (C) were transiently transfected with specific RNAi oligonucleotides (siTFG) or unrelated oligonucleotides as a negative control (siCTR), together with CFP-LC3B plasmid (visualized in red) and cultured in starved conditions for 40'. Wide-field live-cell imaging of starved cells was taken by cellSens microscope. Representative images of lifespan of both ATG13 (B) and (C) are reported. Images of both ATG13 (B) and DFCP1 (C) forming association with LC3B are also shown. The appearance of LC3B on ATG13 (B) (bottom right) and on DFCP1 (bottom right) (C) puncta was quantified and reported. All values are expressed in seconds (s) as mean ± SEM. Yellow arrowheads point at the DFCP1 and LC3B particles in the first frame from their onset, and white arrowheads and white arrows show omegasomes and autophagosomes as indicated. Statistical analyses were performed by unpaired Student's *t*-test. $*P < 0.05$ and $**P < 0.01$ ($n = 3$ independent experiments, $n = 50$ events/condition analysed). Scale bar 1 μm.

D HeLa cells were transfected as in A). Cells were imaged by TEM. Representative electron micrographs (x26500) are reported. The average number of abnormal structures per cell is shown (bottom graph). N, nucleus; M, mitochondria; and ER, endoplasmic reticulum. The average number of abnormal vacuoles per cell was evaluated (upper right). Statistical analysis was performed by unpaired Student's *t*-test. $***P < 0.001$. A minimum of 50 cells were observed. Cell count was performed ($n = 3$ independent experiments, $n \geq 51$ cells analysed). Data are presented as mean ± SEM. Scale bar 500 nm as indicated.

E HeLa cells stably expressing GFP-ATG13 and CFP-ATG16 were transiently co-transfected with DsRed-Rab7 and TFG siRNA (siTFG). Cells were cultured in starved conditions for 1 h. Representative electron micrographs (x3900) and merge of the three fluorophores CLEM are shown. Micrographs at higher magnification (x13500) of a region showing the three fluorophores split and merged are reported. Scale bars: 5 μm upper panels, 1 μm bottom panels.

F Control (TFG-WT) and patient's (TFG-R106C) fibroblasts were grown in fed or starvation conditions in the presence or absence of CLQ for 1 h and then lysed. Protein extracts were analysed by WB to detect ACTIN and LC3B-II as indicated. Densitometry analysis of LC3B-II over ACTIN is shown (right). All data are expressed as the mean ± SEM. Statistical analysis was performed by two-way ANOVA followed by Tukey's multiple comparison test. $*P < 0.05$ and $***P < 0.001$ ($n = 3$ independent experiments).

G Control (TFG-WT) and patient's (TFG-R106C) fibroblasts were grown in fed or starvation conditions for 1 h. Cells were fixed, permeabilized and labelled with anti-ULK (red) antibody. Hoechst was used to stain nuclei. The average of ULK1 puncta number per cell is shown (right). All data are expressed as the mean value ± SEM. Statistical analysis was performed by two-way ANOVA followed by Tukey's multiple comparison test. $*P < 0.05$; $***P < 0.001$; and $****P < 0.0001$ ($n = 3$ independent experiments, $n \geq 14$ fields analysed). Scale bar 5 μm.

Source data are available online for this figure.

Guerroué *et al,* 2017; Wetzel *et al,* 2020). LC3C is described in such reports as a key factor in regulating various selective autophagy processes. Here we demonstrate a role for the axis TFG-LC3C in regulating starvation-dependent autophagy. Indeed, disruption of the TFG-LC3C interaction influences ULK1 protein levels, puncta formation and distribution and consequently autophagy progression, similarly to TFG depletion. Most likely, this interaction is also functional for a proper localization of early autophagy proteins and for the correct recruitment of LC3B to the IM. Another interesting finding is that TFG favours both ULK1-LC3C and ULK1-GABARAP interaction. ULK1 complex members (ULK1, ATG13 and FIP200) bind strongly GABARAP, GABARAP-L1, GABARAP-L2 and LC3C, and weakly LC3A and LC3B (Alemu *et al,* 2012). We could thus speculate that LC3C may cooperate with TFG as a recruiting anchor at the omegasome sites for autophagosome formation and that the TFG-LC3C interaction could be crucial in globally regulating ULK1 during autophagy.

Interestingly, from a biomedical viewpoint, emerging evidence shows a tight correlation between inherited neuropathy-associated genes and autophagy alteration. In particular, mutations in *RAB7* (protein required for autophagosome and lysosome fusion) cause CMT2B neuropathy (Verhoeven *et al,* 2003), and CMT2B patients carrying the V162M *RAB7A* mutation show alteration in autophagy flux. In addition, the function of TECPR2 in maintaining ER export and the formation of early autophagosome intermediates is disrupted by HSP-causing mutations and this, in turn, causes an autophagy impairment (Stadel *et al,* 2015). Of note, several mutations in TFG (such as R106C, G269V and P285L) have been demonstrated to cause different neuropathologies (HSP, CMT2 and HMSN-P). The R106C TFG mutant induces defects in the octamer assembly, impairing the TFG structure; the G269V TFG mutant produces cytoplasmic aggregates, which would trap wild-type TFG. Last, Ishiura and colleagues demonstrated that motor neurons in HSMN-P of patients show TFG/ubiquitin- and/or TDP-43 (TAR DNA-binding protein 43 kDa) immunopositive cytoplasmic inclusions (Ishiura *et al,* 2012). The finding that HSP patient fibroblasts carrying mutated TFG display reduced autophagy levels, defective ULK1 puncta turnover and abnormal structures in the cytoplasm highlights the importance of our discovery in biomedicine. In the case investigated, defective autophagy could be postulated as a possible contributor to ontogenesis or progression of the HSP disease; in particular, neurons are sensitive to accumulation of protein aggregates or damaged organelles and altered autophagy is now recognized as an important cause of neuronal degeneration in both central and peripheral nervous system. In sum, the role of TFG in autophagy could thus be key in a novel pathogenic mechanism for neuropathy associated with its mutation, and our study supports the idea that targeting autophagy may represent a potential approach to improve patients conditions.

Finally, TFG has been found to play a role in oncogenesis, especially as a fusion protein; moreover, several reports suggest that TFG alone could act both as a tumour suppressor and an oncogene, although its role in this context remains unclear (Chen & Tseng, 2014). The fusion partners of TFG include NTRK1 or ALK, and this results in the generation of an oncogene. Interestingly, in both instances, a role for TFG in targeting kinase activities of NTRK1 and ALK to ER exit sites has been found and this, in turn, causes tumour transformation. It would be thus of the highest interest to study a role for TFG-fusion proteins in autophagy mis-regulation, a condition well known to affect cancer cell survival.

 © 2021 The Authors

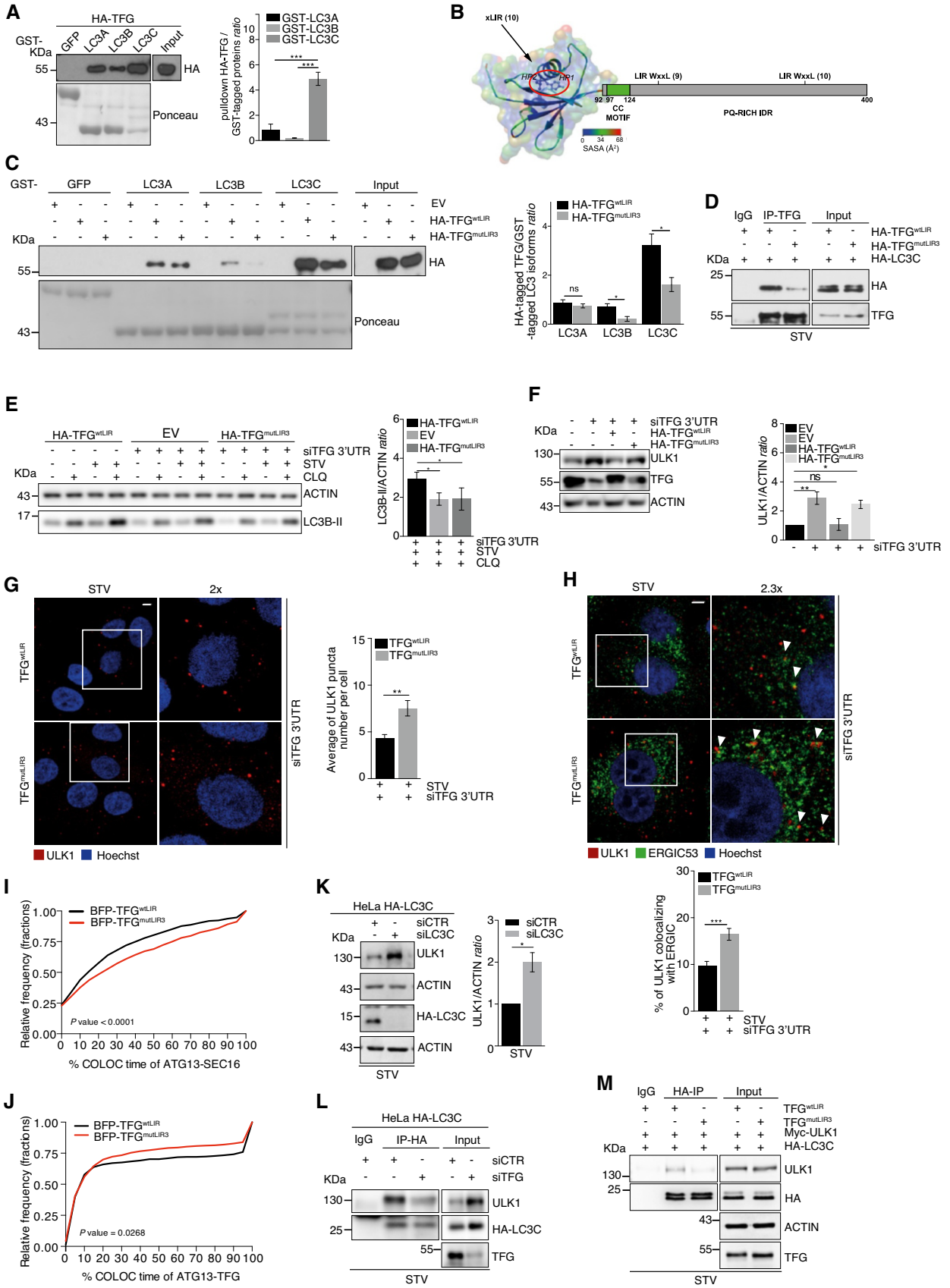
A
HA-TFG
GST-
GFP
LC3A
LC3B
LC3C
Input
KDa
55
43
HA
Ponceau
pulldown HA-TFG / GST-tagged proteins ratio
GST-LC3A
GST-LC3B
GST-LC3C
B
xLIR (10)
HP2
HP1
LIR WxxL (9)
LIR WxxL (10)
92 97 124
400
CC MOTIF
PQ-RICH IDR
SASA (Å²)
C
EV
HA-TFGwtLIR
HA-TFGmutLIR3
HA-TFGwtLIR
HA-TFGmutLIR3
HA-tagged TFG/GST -tagged LC3 isoforms ratio
ns
LC3A
LC3B
LC3C
D
IgG
IP-TFG
Input
HA-TFGwtLIR
HA-TFGmutLIR3
HA-LC3C
25
55
HA
TFG
STV
E
HA-TFGwtLIR
EV
HA-TFGmutLIR3
siTFG 3'UTR
STV
CLQ
43
17
ACTIN
LC3B-II
LC3B-II/ACTIN ratio
F
siTFG 3'UTR
HA-TFGwtLIR
HA-TFGmutLIR3
130
55
43
ULK1
TFG
ACTIN
ULK1/ACTIN ratio
ns
G
STV
2x
TFGwtLIR
TFGmutLIR3
siTFG 3'UTR
Average of ULK1 puncta number per cell
ULK1
Hoechst
H
STV
2.3x
ULK1
ERGIC53
Hoechst
% of ULK1 colocalizing with ERGIC
I
BFP-TFGwtLIR
BFP-TFGmutLIR3
Relative frequency (fractions)
P value < 0.0001
% COLOC time of ATG13-SEC16
J
BFP-TFGwtLIR
BFP-TFGmutLIR3
Relative frequency (fractions)
P value = 0.0268
% COLOC time of ATG13-TFG
K
HeLa HA-LC3C
siCTR
siLC3C
130
43
15
ULK1
ACTIN
HA-LC3C
ACTIN
ULK1/ACTIN ratio
STV
L
HeLa HA-LC3C
IgG
IP-HA
Input
siCTR
siTFG
130
25
55
ULK1
HA-LC3C
TFG
STV
M
IgG
HA-IP
Input
TFGwtLIR
TFGmutLIR3
Myc-ULK1
HA-LC3C
130
25
43
55
ULK1
HA
ACTIN
TFG
STV

Figure 5.

Figure 5. The role of TFG in autophagy requires its LIR-dependent association with LC3C.

A Pulldown assay was performed incubating purified GST-tagged LC3 (A, B and C) isoforms and HA-TFG-transfected HeLa cell lysates. HA-TFG protein levels were analysed by WB; LC3 isoforms and GFP are shown in the Ponceau staining. Densitometry analysis of TFG over GST-tagged LC3 isoforms is reported in the graph (right). Data are expressed as mean ± SEM. Statistical analysis was performed by one-way ANOVA followed by Tukey's multiple comparison test. ***$P < 0.001$ ($n = 3$ independent experiments).

B The model illustrates the domain composition of TFG, including a PB1 domain (residues 10–91), a coiled-coil motif (CC, residues 97–124) and a C-terminal region including a proline–glutamine-rich mostly disordered region. The location of the predicted LIR motifs is also reported, along with the associated PSSM scores from iLIR. The model of the 3D structure of the PB1 domain is coloured according to the solvent accessibility of each residue as derived by Chimera, and the residues for the predicted LIR motif 31–36 for HP1 and HP2 hydrophobic pockets of LC3 proteins are highlighted as sticks.

C Pulldown assays were performed by using purified GST-LC3 (A, B and C) isoforms, each incubated together with empty vector (EV) or HA-TFG^{wtLIR}- or HA-TFG^{mutLIR3}-transfected HeLa cell lysates, respectively. Ponceau staining reports GST-LC3 isoforms and GST-GFP used as a negative control. WB analyses show HA-TFG^{wtLIR} or HA-TFG^{mutLIR3} in the pulldown and in total extracts (Input). Densitometry analyses of HA-tagged TFG normalized over GST-tagged LC3 isoforms (Ponceau) were performed and reported (right). Data are mean value ± SEM. Statistical analysis was performed by multiple *t*-test. *$P < 0.05$ and ns, not significant ($n = 3$ independent experiments).

D HeLa cells were co-transfected with HA-LC3C together with HA-TFG^{wtLIR} or HA-TFG^{mutLIR3} plasmids. After 30' of starvation, protein extracts were immunoprecipitated using an anti-TFG antibody or IgG as a negative control. LC3C and TFG were analysed by WB.

E HeLa cells were co-transfected with 3'UTR TFG siRNA together with HA-TFG^{wtLIR} or an empty vector (EV) or TFG^{mutLIR3} plasmids, expressed at near endogenous levels. Cells were cultured with complete or starvation (STV) media and grown in the presence or absence of CLQ for 1 h. ACTIN and LC3B-II protein levels are shown. Densitometry analysis of LC3B-II over actin for indicated conditions is shown in the graph (right). Data are mean value ± SEM. Statistical analysis was performed one-way ANOVA followed by Dunnett's multiple comparison test. *$P < 0.05$ ($n = 3$ independent experiments).

F HeLa cells were co-transfected with unrelated oligonucleotides as a negative control (siCTR) and empty vector (EV) or 3'UTR siRNA TFG siRNA together with EV or HA-TFG^{wtLIR} or TFG^{mutLIR3} plasmids, expressed at near endogenous levels. Protein extracts were analysed by WB to detect ULK1, TFG and ACTIN as indicated. Densitometry analysis of ULK1 over ACTIN is shown (right). Data are mean value ± SEM. Statistical analysis was performed by one-way ANOVA followed by Dunnett's multiple comparison test. *$P < 0.05$; **$P < 0.01$; and ns, not significant ($n = 4$ independent experiments).

G, H HeLa cells stably expressing untagged TFG^{wtLIR} or TFG^{mutLIR3} were transfected with 3'UTR TFG siRNA, starved for 1 h, fixed, permeabilized and immunolabelled with ULK1 (red) alone or ULK1 (red) and ERGIC53 (green) (H). Hoechst was used to stain nuclei. ULK1 puncta number (G) was analysed and reported as mean ± SEM in the graph (right) ($n = 3$ independent experiments, $n = 24$ fields analysed). Co-localization analyses between ULK1 (red) and ERGIC53 (green) (H) were performed by Jacop plugin. Values of Mander's coefficient for ULK1, expressed as percentage, are reported as mean ± SEM (bottom graph) ($n = 3$ independent experiments, $n = 19$ fields analysed). White arrowheads point at co-localization events between ULK1 and ERGIC53. Statistical analyses were performed by unpaired Student's *t*-test. **$P < 0.01$ and ***$P < 0.001$. Scale bar 5 μm.

I HeLa cells stably expressing GFP-ATG13 together with BFP-TFG^{wtLIR} or BFP-TFG^{mutLIR3} were co-transfected with a siRNA targeting endogenous TFG (siTFG 3'UTR) and mCherry-SEC16 plasmid and then cultured for 40' with starvation medium. Cells were visualized with cellSens microscope for live-cell imaging. Analysis of the percentage of GFP-ATG13 lifetime co-localizing with mCherry-SEC16 in the presence of TFG^{wtLIR} or TFG^{mutLIR3} is reported in the cumulative relative frequency plot. Statistical analysis was performed by Kolmogorov–Smirnov test. $P < 0.0001$ ($n = 3$ independent experiments, $n \geq 995$ number of co-localization events analysed).

J HeLa cells stably expressing GFP-ATG13 together with BFP-TFG^{wtLIR} or BFP-TFG^{mutLIR3} were transfected with 3'UTR TFG siRNA to downregulate endogenous TFG. Cells were cultured for 40' with starvation medium and visualized with cellSens microscope for live-cell imaging. Analysis of the percentage of GFP-ATG13 lifetime co-localizing with BFP-TFG^{wtLIR} or BFP-TFG^{mutLIR3} is reported in the cumulative relative frequency plot. Statistical analysis was performed by Kolmogorov–Smirnov test. $P = 0.0268$ ($n = 3$ independent experiments, $n \geq 379$ number of co-localization events analysed).

K HeLa cells harbouring endogenously HA-tagged LC3C were transfected with specific RNAi oligonucleotides (siLC3C) or unrelated oligonucleotides as a negative control (siCTR) and cultured in starvation medium for 30'. Protein extracts were analysed by WB to detect ULK1, ACTIN and HA-LC3C as indicated. Densitometry analysis of ULK1 over ACTIN is reported (right). Data are expressed as mean ± SEM. Statistical analysis was performed by unpaired Student's *t*-test. *$P < 0.05$ ($n = 3$ independent experiments).

L HeLa cells harbouring endogenously HA-tagged LC3C were transfected with a siRNA targeting TFG (siTFG) or with a non-targeting control (siCTR). After 30' of starvation, cells were lysed, and protein extracts were immunoprecipitated by using an anti-HA antibody or IgG as negative control. Protein extracts were analysed by WB to detect ULK1 and HA-LC3C as indicated.

M HeLa cells stably expressing untagged TFG^{wtLIR} or TFG^{mutLIR3} were co-transfected with HA-LC3C and Myc-ULK1 plasmids as indicated. Cells were starved for 30', and protein extracts were immunoprecipitated using an anti-HA antibody or IgG as negative control. Protein extracts were analysed by WB to detect ULK1, HA-LC3C, TFG and ACTIN as indicated.

Source data are available online for this figure.

Materials and Methods

Human subjects

All procedures performed in studies involving human participants were in accordance with the ethical standards of the institutional and/or national research committee and with the 1964 Helsinki declaration and its later amendments or comparable ethical standards.

Skin biopsies were performed after obtaining informed consent approved by the Ethics Committee of Fondazione IRCCS Istituto Neurologico Carlo Besta.

Cell culture and treatments

HeLa and HEK293 cells were cultured in DMEM (EuroClone, ECB7501L) supplemented with 10% foetal bovine serum (FBS) (GIBCO, 10270106), 2 mM L-glutamine (EuroClone, ECB3000D) and 1% penicillin/streptomycin (EuroClone, ECB3001B) solution. HEK293 cells stably expressing GFP-ATG13 or GFP-DFCP1 were also selected in 800 mg/ml Geneticin (GIBCO, 11811031). HeLa cells harbouring endogenously HA-tagged LC3C, GABARAP, GABARAPL1 and GABARAPL2 were cultured in DMEM with 10% FBS, 5% glutamine and selected in 4 μg/ml of blasticidin (GIBCO, A1113903). Cells were maintained in a humidified atmosphere containing 5% CO_2 at

 © 2021 The Authors

Table 1. Oligonucleotides related to the experimental procedures

Thermo Fisher Scientific	TFG	5′-ACAGCAGUACCAGGCGAGCAAUUAU-3′
		5′-AUAAUUGCUCGCCUGGUACUGCUGU-3′
Sigma-Aldrich	TFG-3′UTR	5′-CCAAAAGACUCCAGUACUA-3′
		5′-UAGUACUGGAGUCUUUUGG-3′
Thermo Fisher Scientific	SEC23A	5′-GGGUGAUUCUUUCAAUACU-3′
		5′-AGUAUUGAAAGAAUCACCC-3′
Sigma-Aldrich	SEC16	5′-CCCAAGACUGCAGAACCCAGCUAUU-3′
		5′-GCAGCUCUGGAACUUAGUA-3′
Sigma-Aldrich	ULK1	5′-GAGAACGUCACCAAGUGCAAGCUGU-3′
		5′-ACAGCUUGCACUUGGUGACGUUCUC-3′
Thermo Fisher Scientific	MAP1LC3C	5′-GCUUGGCAAUCAGACAAGAGGAAGU-3′
		5′-ACUUCCUCUUGUCUGAUUGCCAAGC-3′
Sigma-Aldrich	MAP1LC3B	5′-CUCCCUAAGAGGAUCUUUAUU-3′
		5′-AAUAAAGAUCCUCUUAGGGAG-3′
Sigma-Aldrich	GABARAP	5′-GGUCAGUUCUACUUCUUGA-3′
		5′-UCAAGAAGUAGAACUGACC-3′
Horizon/ Dharmacon	GABARAPL1	5′-CUAGUGCCCUCUGACCUUA-3′
		5′-UAAGGUCAGAGGGCACUAG-3′
Sigma-Aldrich	GABARAPL2	5′-UGGGCUAGGUGCACCGUAA-3′
		5′-UUACGGUGCACCUAGCCCA-3′,

37°C. The induction of autophagy by nutrients starvation was obtained washing the cells with phosphate-buffered saline (PBS) (EuroClone, ECB4053) and incubating with Earle's balanced salt solution (EBSS; Sigma-Aldrich, 254134) for the indicated time periods. Autophagy induction of HEK293 or HeLa cells for live imaging experiments was accomplished washing three times with pre-warmed starvation medium (140 mM NaCl, 1 mM $CaCl_2$, 1 mM $MgCl_2$, 5 mM glucose, 1% bovine serum albumin (BSA; Sigma-Aldrich A9647) and 20 mM Hepes pH 7.4) and incubating at 37°C under 5% CO_2 for 40 min. Lysosome activity was inhibited for 1 h with 20 μM CQ (Sigma-Aldrich, C6628) or with 10 mM NH_4Cl (Sigma-Aldrich, 254134) or with 100 nM of bafilomycin A1 (Baf A1) (Selleck chemicals, S1413) for the indicated time periods. Protein translation was inhibited using 50 μg/μl cycloheximide (CHX; Sigma-Aldrich, C4859). All used cell lines were transiently transfected with Lipofectamine 2000 (Thermo Fisher Scientific, 11668-019) according to the manufacturer's instructions. Patient fibroblasts and control were obtained from skin biopsy as previously reported (Catania *et al,* 2018). All experiments were performed on cells at the same passage number. Cell lines were regularly tested and verified to be mycoplasma negative by PCR; all cell lines tested negative for mycoplasma.

Plasmids and retroviral transduction

Plasmid encoding for wild-type Myc-ULK1 was provided by S.A. Tooze (The Francis Crick Institute, Lincoln's Inn Fields Laboratories, London, England, UK). DsRed-rab7WT plasmid was by Addgene (#12661). Vectors encoding for GST-GFP, GST-LC3A, GST-LC3B, GST-LC3C, HA-LC3A, HA-LC3B and HA-LC3C were a kind gift from C. Behrends. HeLa cell lines harbouring endogenously HA-tagged LC3C, or GABARAP, or GABARAPL1, or GABARAPL2 were obtained as previously described (Le Guerroué *et al,*2017). GST-GABARAP, GST-GABARAPL1 and GST-GABARAPL2 were a gift from I. Dikic (Institute of Biochemistry II, Goethe University, Frankfurt Germany). Plasmid encoding for CFP-LC3B, mCerry-SEC16 together with HEK293 cells stably transfected with GFP-ATG13 or GFP-DFCP1 vectors were provided by N.T. Ktistakis (Babraham Institute, Cambridge, UK). To obtain pCI-HA-TFG plasmid, TFG was cleaved from pcDNA3-TFG by KpnI/NotI and was sub-cloned to the pCI-HA vector purchased from Addgene. TFG mutant constructs were generated by using the site-directed mutagenesis kit (Agilent Technologies, 200518). The sequences used are as follows: pCI HA-TFG^{R106C} R to C: 5' CAAGTCAGGTGAAATATCTC TGT CGAGAACTGATAG AACT 3'. pCI HA-$TFG^{mutLIR2}$: F to A, 5′-GGCAGCAAGTATGTCTG CTGCTGATCCTTTAAAAAACCAAG-3′; L to A, 5′-GGCAGCAAGTA TGTCTGCTGCTGATCCTGCAAAAAACCAAG-3′. pCI HA-$TFG^{mutLIR3}$: F to A, 5′-ATCAACCAAGACCAGGTGCTACTTCACTTCCTGGAAG-3′; L to A, 5′-CCAGGTGCTACTTCAGCTCCTGGAAGTACCATG-3′. To obtain stable cell lines, TFG^{wtLIR} and $TFG^{mutLIR3}$ were sub-cloned into the SFG (Quintarelli *et al,* 2018) retrovirus vector in frame with the 2A sequence and the truncated cell-surface CD19 selectable marker. Then, the retroviral supernatants were produced in 293T cells, as previously described (Caruana *et al,* 2015). For live-cell imaging or CLEM analysis, stable cell lines were obtained using the following vectors: TFG^{wtLIR} and $TFG^{mutLIR3}$ sub-cloned into pMSCV-IRES-Blue FP (Addgene #52115), pMRX-IP/SECFP-ATG16A1 (Addgene #58994) and pMXs-IP-EGFP-ATG13 (Addgene #38191), as described in the figure legends.

RNA Interference (RNAi)

RNAi was achieved by RNA oligonucleotide duplex listed in Table 1.

2.5×10^5 cells per well were transfected with 100 pmol siRNA oligos in six-well plates using Lipofectamine 2000 following the manufacturer's instructions

Western blot analysis

Cells were rinsed in PBS on ice and lysed in RIPA buffer (50 mM Tris–HCl pH 7.4, 150 mM NaCl, 1 mM EDTA, 5 mM $MgCl_2$ 1% Triton X-100, 0,25% sodium deoxycholate and 0,1% SDS) plus protease inhibitor cocktail (Sigma-Aldrich, P8340), Na_4VO_3 0.1 mM (Sigma-Aldrich, S6508), NaF 1 mM (Sigma-Aldrich 201154) and β-glycerophosphate 5 mM (Sigma-Aldrich G9422).

Cell extracts were centrifuged at 13,000 rpm for 10 min at 4°C. Protein concentrations were determined with the Bio-Rad Protein Assay Kit (Bio-Rad, 5000113 and 5000114). Cell extracts or immunoprecipitates were denatured by adding 1 volume of 4 × Laemmli SDS sample loading buffer with β-mercaptoethanol and boiled at 95°C for 10 min. Then, proteins were separated by SDS–PAGE. PVDF (Merck Millipore, IPVH00010) membranes were incubated with primary antibodies followed by horseradish peroxidase-conjugated secondary antibody (Bio-Rad, rabbit 1706515, mouse 1706516) and visualized with ECL (Merck Millipore, WPKLS0500). Densitometry analysis was performed using ImageJ software. Comparison between control and sample in the WB intensity measurement was made from the same WB. Of note, in some cases, WB was captured using digital cameras (Alpha Innotech FluorChem SP, or iBright FL1500), whereas

© 2021 The Authors

others were captured on film (Aurogene, AU1102). Backgrounds in WB images from different experimental approaches were then equalized by changing their exposition post-acquisition.

Antibodies

The primary antibodies used in this study were as follows: mouse anti-HA tag (Santa Cruz Biotechnology, sc-7392) and rabbit anti-HA tag antibody (Santa Cruz Biotechnology, sc-805), rabbit anti-HA (Cell Signaling Technology, #3724), mouse anti-TFG (Santa Cruz Biotechnology, sc-515054) and rabbit anti-TFG (Santa Cruz Biotechnology, sc-98969), rabbit anti-TFG (Abcam, ab156866), mouse anti-TFG (Novus Biological, NBP2-62212), mouse anti-Myc (9E10) (Santa Cruz Biotechnology, sc-40), rabbit anti-LC3-XP (D11) (Cell Signaling Technology, #3868), mouse LC3B (5F10) (Nanotools, 0231-100), rabbit anti-ULK1 (D8H5) (Cell Signaling Technology, #8054), rabbit anti-ULK1 (N-17) (Santa Cruz Biotechnology, sc-10900), mouse anti-GOLGIN-97 (CDF4) (Thermo Fisher Scientific, A-21270), rabbit anti-ATG16L1 (D6D5) (Cell Signaling Technology, #8089), rabbit ATG9A (D4O9D) (Cell Signaling Technology, #13509) rabbit anti-ATG13 (E1Y9V) (Cell Signaling Technology, #13468), mouse anti-ATG13 (2H4.2) (Merck Millipore, MABC46), rabbit anti-pS318-ATG13 (Rockland, 600-401-C49), rabbit anti-ATG14 (Cell Signaling Technology, #5504) rabbit pS29-ATG14 (Cell Signaling Technology, #13155), rabbit anti-Actin (Sigma-Aldrich, A2066), rabbit anti-GADPH (Sigma-Aldrich, G9545), mouse anti-Calnexin (AF18) (Santa Cruz Biotechnology, sc-23954), mouse anti-SEC31A (BD, 612350) rabbit anti-SEC23A (Cell Signaling Technology, #8162) and mouse anti-ERGIC53 (Enzo Life Science, ABS300-0100). All antibodies are listed in Table EV2.

Immunoprecipitation assay

HeLa cells were rinsed with ice PBS and lysed in NP-40 lysis buffer (50 mM Tris–HCl pH 7.4, 150 mM NaCl, 0.5% NP-40 and protease inhibitor cocktail (Sigma-Aldrich, P8340)) or with a buffer used for co-IP with ATG8 proteins (10 mM Tris–HCl pH 7.4, 100 mM NaCl, 2 mM EDTA, 1% NP-40). For endogenous co-IP, was used a buffer containing 40 mM Hepes pH 7.4, 2 mM EDTA and 0,3% chaps, and for IP washes was added 150 mM of NaCl. IP assays were performed with 0.5 mg of lysates for co-IP in overexpression, 1.5 mg of lysates for co-IP in semi-endogenous conditions and 2 mg of lysate in endogenous conditions. Lysates were then incubated with 1 μg, 1.5 μg or 2 μg, respectively, of indicated primary antibody at 4°C with rotation overnight (O/N) before addiction of 15 μl dynabeads protein G (Invitrogen, 10003D) and then incubated at 4°C for 1 h. Immunoprecipitates were then washed 5 × 5 min with its own lysis buffer or wash buffer and then denatured by adding 1 volume of 4 × Laemmli SDS sample buffer (Thermo Fisher Scientific, NP0007) with β-mercaptoethanol and incubated at 95° for 10 min.

Pulldown assay

Recombinant GST-fusion proteins were expressed in *E. coli* BL21 (DE3) (Promega, L1195) using 0.5 mM IPTG at 25°C O/N. Bacteria were lysed in NET-N buffer (20 mM Tris–HCl, pH 8.0, 100 mM NaCl, 1 mM EDTA, 0.5% Nonidet P-40) containing EDTA-free protease inhibitor mixture (Sigma-Aldrich, P8465) and subjected to sonication. GST proteins were purified and immobilized on glutathione agarose (Thermo Scientific, 16100). HA-TFG^{wtLIR} or HA-TFG^{mutLIR3} or positive control (supplementary Fig 5E and F) vectors were transiently transfected in HeLa cells as indicated. Then, cells were lysed with NET-N buffer. GST pulldown assays were performed by incubating immobilized GST-fusion proteins with protein extract derived from HeLa cells for 2 h at 4°C with gentle agitation. Unbound proteins were removed by washing the resins five times with NET-N buffer. GST proteins were eluted from the beads with 10 mM reduced glutathione in 50 mM Tris–HCl (pH 8.0), for 30 min with gentle agitation at room temperature. The eluted samples were boiled for 5 min in sample loading buffer and separated by SDS–PAGE.

Immunofluorescence analysis

Cells were washed in PBS and fixed with 4% paraformaldehyde in PBS for 10 min. After permeabilization with 0.4% Triton X-100 (Sigma-Aldrich, X-100, T9284) in PBS for 5 min. For LC3 staining, cells were fixed and permeabilized with cold methanol for 10' at −20°. Coverslips were incubated for 1 h with 3% normal goat serum (Sigma-Aldrich, NS02L) for blocking non-specific signals. Cells were incubated (O/N) at 4°C with primary antibodies and 1% normal goat serum. Cells were then washed with PBS and incubated for 1 h and labelled with anti-mouse (Thermo Fisher Scientific, A11017, A21425) or anti-rabbit (Thermo Fisher Scientific A21430, A11070) secondary antibodies. Nuclei were stained with 1 μg/ml Hoechst for 5 min at room temperature. Images were obtained by several confocal microscopes, depending of hosting laboratory: Olympus FV1000 laser-scanning confocal microscope, equipped with a 60x (NA 1.35) oil immersion objective (Tor Vergata University, Rome), Leica TCS-SP8X laser-scanning confocal microscope equipped with a 60x (NA 1.4) oil immersion objective (Bambino Gesù Pediatric Hospital, Rome) and Carl Zeiss LSM 780 Confocal 60x (NA 1.4) oil immersion objective and N-Nikon Structured Illumination Microscopy (N-SIM) with 100x (NA 1.49) oil immersion objective with lateral resolution of 120 nm (Babraham Institute, Cambridge). Image analysis has been performed using "Fiji" (Fiji Is Just ImageJ) open-source software. Co-localization analysis was performed by using "Jacop plugin". For all co-localization analyses, to evaluate the percentage of ULK1 puncta localized to several intracellular structures or particles, Mander's coefficient was used. Images were processed to equally remove the background without affecting the original signal. Co-localization values were represented as a percentage of pixels of a channel overlapping with the other channel. All acquisitions were performed in non-saturated single focal central planes, and images were captured from randomly selected fields of view.

Live-cell imaging and analysis of live-cell imaging movies

Olympus cellSens, a wide-field imaging system, with a 100x oil immersion objective and a sCMOS camera was used to capture images of live cells in Babraham Institute, Cambridge, for Fig 4B and C. Olympus cellSens with a 100x oil immersion objective and a CCD camera was used to capture images of live cells in the University of Ferrara, Italy, for the analysis in Fig 5I and J. HEK293 cells stably expressing GFP-ATG13 or GFP-DFCP1, or HeLa cells stably expressing GFP-ATG13 and BFP-TFG^{wtLIR} or GFP-ATG13 and BFP-TFG^{mutLIR3} were plated onto 60-mm dishes and transiently co-

 © 2021 The Authors

transfected with the indicated plasmids together with indicated siRNAs. Transfected cells were transferred onto 22-mm-diameter glass coverslips (BDH) and on the third day, the individual coverslips were secured in an imaging chamber with 2 ml of starvation medium. The assembled imaging chamber was secured onto the microscope stage, and cells were maintained at 37°C in the incubation system of cellSens microscope. Each movie is composed of 240 pictures (frames) each taken every 10 s. Live-cell imaging movies were analysed by Fiji, a Java-based image processing program.

Autophagy dynamics analysis

Analysis of dynamics between autophagy proteins was performed by the examination of 50 events deriving from three independent experiments. The events analysed are characterized by the number of frames, expressed in seconds, from the moment at which the analysed particles (GFP-ATG13 and GFP-DFCP1) are clearly emerging to the collapse. Events corresponding to particles moving out of focus and then back in were excluded from the analysis. Same type of analysis was performed for the CFP-LC3 (visualized in red); in this case, we analysed just the moment in which CFP-LC3 structures appeared on GFP-ATG13 or GFP-DFCP1 particles taking advantage of coordinates of these particles.

ATG13 tracking and particles-proximity analysis

Time-lapse images of GFP-ATP13 and BFP-TFG or mCherry-SEC16 were processed and quantified using open-source software Fiji (Fiji – ImageJ). Images were first corrected for noise suppression and background subtraction using a median filter (kernel size 2 pixels) and a rolling ball algorithm (kernel size 150 pixels), respectively. As no significant changes in total fluorescence intensity per field of view were expect apart from fluorescence degradation, time-lapse stacks were corrected for photobleaching using the simple-ratio method. Eventual lateral shifts were corrected using the MultiStackReg plugin, and the shift was detected as translation of the GFP-ATP13 channel and then re-applied to the other channels. Finally, dot-shaped structures were emphasized using a 2D top-hat algorithm (kernel size 7x7). After image processing, GFP-ATP13 puncta were tracked using the TrackMate plugin. LoG detector and simple LAP tracer were used for spot detection and tracking, respectively. Of all detected tracks, those starting at timepoint < 2 or > 238 were discarded to ensure that all particles were tracked in the entirety of their lifetime. All tracks with lifetime shorter than nine frames were considered non-specific or partial detection then discarded. At the end of the detection, gaps were filled with spots and spot size was automatically re-calculated. Fluorescence intensity for each fluorescence channel on each track was exported and analysed with Excel. To identify frames were GFP-ATP13 co-localized with BFP-TFG or mCherry-Sec16, maximum fluorescence intensity of the non-GFP channel from all the timepoints of all the tracks was summarized. Then considering that pixel size was set below optical resolution, a timepoint where the maximum fluorescence intensity doubled the median of the distribution was considered as co-localized.

Correlative Light Electron Microscopy (CLEM) and Transmission Electron Microscopy (TEM)

Cells stably expressing CFP-ATG16L1 and GFP-ATG13 were transfected as indicated. Cells were plated in 30-μm Grid-500 glass bottom dish (ibidi #81168) (18×10^3 cells / dish) and after 24 h were starved (EBSS) or not for 1 h. After treatment, cells were fixed with 3,7% paraformaldehyde (PFA) in PBS for 1 h at RT. Cell orientation and position in the 30-μm Grid-500 glass bottom dish (ibidi #81168) were identified and images acquired by using a confocal inverted microscope (Leica) TCS SP5 II, HC PL FLUOTAR 20X NA 0.50 or 63X NA 0.80 oil objective. After image acquisition, cells for CLEM and TEM were processed in parallel by fixation with 2.5% glutaraldehyde in 0.1 M sodium cacodylate buffer pH 7.4, 1 h at RT. After washing with 0.1 M cacodylate buffer, cells were treated with 1% osmium tetroxide plus potassium ferrocyanide 1% in 0.1 M sodium cacodylate buffer for 1 h at 4°C. The samples were then rinsed, dehydrated in a series of graded ethanol and embedded in an epoxy resin (Sigma). Ultrathin sections of the embedded samples (60–70 nm) were obtained by using an Ultrotome V (LKB) ultramicrotome and were counterstained with uranyl acetate and lead citrate. The sections were finally analysed using a Tecnai G2 (FEI) transmission electron microscope operated at 100 kV. The images were captured with a Veleta (Olympus Soft Imaging System) using 2.800X, 3.900X or 13.500X magnification of the sections.

The images obtained by fluorescence and electron microscopy were aligned using ImageJ. For overlapping, the nucleus and reference structures were taken as reference and different magnifications adapted to the scale bars.

qPCR

Total RNA was isolated by using RNeasy mini kit (QIAGEN, 217004). One μg RNA was retrotranscribed using M-MLV enzyme and oligodT (Promega, C1101). qPCR was performed using SYBR Green PCR Master Mix Applied Biosystems (Thermo Fisher Scientific, 4309155) with the QuantStudio 12K Flex Applied Biosystems. The following oligonucleotide primers were used for LC3C: (LC3C#1: 5'-TGCCGGTGATAGTAGAAA-3'; 5'-GGTGTTCCTGGTAC AGCT-3' and LC3C#2: 5'-TGACCATGACCCAGTTCC-3'; 5'-TCCT CATCCTTGTAGTCTCT-3'), and for β2m: (5'-CTCCGTGGCCTTA GCTGTC-3'; 5'-TCTCTGCTGGATGACGTGAG-3'). The mRNA expression of the gene of interest was normalized to β2m expression, and the ΔΔCt method was used; mRNA levels were then normalized to the control conditions.

LIR prediction

We predicted the possible LIRs of TFG with *iLIR* and associated PSSM scores (Jacomin *et al*, 2016). For each LIR, we assessed the propensity to be located in disordered regions with *MobiDB* (Piovesan *et al,* 2018) and other structural properties with *FELLS* (Piovesan *et al,* 2017).

Modelling of PB1 domain of TFG

We used *HHPred* (Söding, *et al,* 2005) to search for templates and the optimal alignment, along with *Modeller* (Webb, & Sali, 2017) to obtain a three-dimensional (3D) model for the TFG PB1 domain. We identified only templates with a sequence identity lower than 20% with respect to the PB1 domain of TFG, which indicates a remote homology with known structures. Among the matches identified by HHPRED, we focused our attention on the PB1 domains from the

© 2021 The Authors

protein kinase C (PDB entry 1WMH, chain B, Hirano *et al*, 2005) for which we obtained a sequence identity of 19% according to the HHPRED alignment (Table S1). The predicted secondary structures for the PB1 domain of TFG using the DSSP algorithm (Zacharias & Knapp, 2014), which is based on intra backbone hydrogen bond networks, matched properly with the known secondary structures of the templates and the gaps in the alignment where less than three residues long and located in disordered regions of the PB1 fold. The quality of the model was evaluated with *VADAR* (Volume Area Dihedral Angle Reporter) (Willard *et al*, 2003) with particular attention to the region where the first predicted LIR motif is located. We estimated the relative solvent accessible surface area of the residues 31–36 using NACESS (http://wolf.bms.umist.ac.uk/naccess/).

Statistical analysis

Densitometry analysis was performed using ImageJ software. All statistical calculations were performed and graphed using GraphPad Prism. Each point value represents the mean ± SEM (as reported in the figure legends). Number of independent experiments and number of replicates used to perform statistics are reported in the figure legends. Statistical significance was measured using an unpaired Student's *t*-test, assuming a two-tailed distribution, one-way and two-way analysis of variance (ANOVA) followed by Tukey's post hoc test or followed by Dunnett's multiple comparison test, or multiple *t*-test, or Kolmogorov–Smirnov test using GraphPad Prism program as reported in the figure legends. Significance is defined as $*P < 0.05$; $**P < 0.01$; $***P < 0.001$; $****P < 0.0001$; and ns, not significant. The source data are available in the supplementary information page.

Data availability

All the data on models and predictions are freely available in the GitHub repository https://github.com/ELELAB/LIR_TFG. All other data required to evaluate the conclusions here presented are in the paper or in Supplementary Materials.

Expanded View for this article is available online.

Acknowledgements
We are grateful to S. Walker for the technical assistance. We thank the "Cell lines and DNA Bank of Genetic Movement Disorders and Mitochondrial Diseases" of the Telethon Network of Genetic Biobanks (grant GTB12001J). Francesco Cecconi's laboratory is supported by grants from the Danish Cancer Society (KBVU R72-A4408, R146-A9364, R231-A14034), the Novo Nordisk Foundation (NNF13OC0007559, NNF16OC0022544), the Lundbeckfonden (R233-2016-3360), the LEO Foundation (LF17024), "Associazione Italiana per la Ricerca sul Cancro" (AIRC project IG 2019 #23543) and The Italian Ministry of Research (MIUR, project PRIN 2017 FS5SHL Radius). F. Cecconi's and E. Papaleo's laboratories in Copenhagen are part of the Center of Excellence for Autophagy, Recycling and Disease (CARD), funded by the Danmarks Grundforskningsfond (DNRF125), Carlsberg fondet Distinguished Fellowship (CF18-0314) to E.P. and a Netaji Subhash ICAR international fellowship (Govt. of India) to M.K. This research was also supported in part by grants from the Italian Ministry of Health (Ricerca corrente) to F. Nazio; the Italian Ministry of Education, University and Research (Research Project of National Relevance 2017 ID 2017WC8499) to F. Locatelli; and AIRC (Associazione Italiana Ricerca sul Cancro, 5x1000 ID 9962 and AIRC IG 2018 ID 21724) to F. Locatelli. This work is in part supported by European Research Council Grant 853057-InflaPML (to C.G.) and EMBO Short-Term Fellowship (number 7463) to M. Carinci. We give a special thanks to Vanda Turcanova for her help with cloning and mutagenesis, and Dr. Cristina Valacca, (Copenhagen) Prof. Silvia Campello, Dr. Valentina Cianfanelli and Dr. Carlo Rodolfo (Rome) for their strenuous help and support. C.B. was supported by the Deutsche Forschungsgemeinschaft (DFG, German Research Foundation) within the frameworks of the Munich Cluster for Systems Neurology (EXC 2145 SyNergy – ID 390857198) and of the Collaborative Research Center 1177 (ID 259130777).

Author contributions
FN and FC conceived the presented idea, developed the theory and, together with MCari, designed the work plan and wrote the paper. FL supervised and supported this work besides providing key intellectual advice. MCari. performed most of the experiments. MB helped with IFs. GM, BT, CF and DC helped with the biochemical assays. LA and IC generated both TFG^{wtLIR} and $TFG^{mutLIR3}$ constructs and produced viruses for all stable cell lines used. RN performed TEM experiments and analyses. MES and MCarr performed TEM and CLEM assays. NTK supervised high-resolution imaging approaches. MBon performed live-cell imaging analysis. FE generated HeLa cell lines harbouring endogenously expresses ATG8 proteins. SP and VD performed confocal images acquisition. MK, ML and EP developed the PB1 model and carried out the bioinformatics analyses. CP and VT provided control' and TFG mutated patient's fibroblasts. PP, CG, CB, FLG, NTK, MM and FL provided critical reagents.

Conflict of interest
The authors declare that they have no conflict of interest.

References

Alemu EA, Lamark T, Torgersen KM, Birgisdottir AB, Larsen KB, Jain A, Olsvik H, Øvervatn A, Kirkin V, Johansen T (2012) ATG8 family proteins act as scaffolds for assembly of the ULK complex: sequence requirements for LC3-interacting region (LIR) motifs. *J Biol Chem* 287: 39275 – 39290

Axe EL, Walker SA, Manifava M, Chandra P, Roderick HL, Habermann A, Griffiths G, Ktistakis NT (2008) Autophagosome formation from membrane compartments enriched in phosphatidylinositol 3-phosphate and dynamically connected to the endoplasmic reticulum. *J Cell Biol* 182: 685 – 701

Beetz C, Johnson A, Schuh AL, Thakur S, Varga R-E, Fothergill T, Hertel N, Bomba-Warczak E, Thiele H, Nürnberg G *et al* (2013) Inhibition of TFG function causes hereditary axon degeneration by impairing endoplasmic reticulum structure. *Proc Natl Acad Sci USA* 110: 5091 – 5096

Birgisdottir ÅB, Lamark T, Johansen T (2013) The LIR motif - crucial for selective autophagy. *J Cell Sci* 126: 3237 – 3247

Caruana I, Savoldo B, Hoyos V, Weber G, Liu H, Kim ES, Ittmann MM, Marchetti D, Dotti G (2015) Heparanase promotes tumor infiltration and antitumor activity of CAR-redirected T lymphocytes. *Nat Med* 21: 524 – 529

Catania A, Battini R, Pippucci T, Pasquariello R, Chiapparini ML, Seri M, Garavaglia B, Zorzi G, Nardocci N, Ghezzi D *et al* (2018) R106C TFG variant causes infantile neuroaxonal dystrophy "plus" syndrome. *Neurogenetics* 19: 179 – 187

Chen Y, Tseng S-H (2014) Targeting tropomyosin-receptor kinase fused gene in cancer. *Anticancer Res* 34: 1595 – 1600

 © 2021 The Authors

Colecchia D, Stasi M, Leonardi M, Manganelli F, Nolano M, Veneziani BM, Santoro L, Eskelinen EL, Chiariello M, Bucci C (2018) Alterations of autophagy in the peripheral neuropathy Charcot-Marie-Tooth type 2B. *Autophagy* 14: 930 – 941

Davis S, Wang J, Zhu M, Stahmer K, Lakshminarayan R, Ghassemian M, Jiang Y, Miller EA, Ferro-Novick S (2016) Sec24 phosphorylation regulates autophagosome abundance during nutrient deprivation. *eLife* 5: e21167

Funderburk, S.F., Wang, Q.J., Yue, Z (2010) The Beclin 1-VPS34 complex–at the crossroads of autophagy and beyond. *Trends Cell Biol* 20: 355 – 362

Gammoh N, Florey O, Overholtzer M, Jiang X (2013) Interaction Between FIP200 and ATG16L1 Distinguishes ULK1 Complex-Dependent and -Independent Autophagy. *Nat Struct Mol Biol* 20: 144 – 149

Gan W, Zhang C, Siu KY, Satoh A, Tanner JA, Yu S (2017) ULK1 phosphorylates Sec23A and mediates autophagy-induced inhibition of ER-to-Golgi traffic. *BMC Cell Biol* 18: 22

Ge L, Melville D, Zhang M, Schekman R (2013) The ER-Golgi intermediate compartment is a key membrane source for the LC3 lipidation step of autophagosome biogenesis. *eLife* 2: e00947

Ge L, Zhang M, Schekman R (2014) Phosphatidylinositol 3-kinase and COPII generate LC3 lipidation vesicles from the ER-Golgi intermediate compartment. *eLife* 3: e04135

Le Guerroué F, Eck F, Jung J, Starzetz T, Mittelbronn M, Kaulich M, Behrends C (2017) Autophagosomal content profiling reveals an LC3C-dependent piecemeal mitophagy pathway. *Mol Cell* 68: 786 – 796

Hanna MG, Block S, Frankel EB, Hou F, Johnson A, Yuan L, Knight G, Moresco JJ, Yates JR, Ashton R *et al* (2017) TFG facilitates outer coat disassembly on COPII transport carriers to promote tethering and fusion with ER–Golgi intermediate compartments. *Proc Natl Acad Sci USA* 114: E7707 – E7716

Harlalka GV, McEntagart ME, Gupta N, Skrzypiec AE, Mucha MW, Chioza BA, Simpson MA, Sreekantan-Nair A, Pereira A, Günther S *et al* (2016) Novel genetic, clinical, and pathomechanistic insights into TFG-associated hereditary spastic paraplegia. *Hum Mutat* 37: 1157 – 1161

Hein MY, Hubner NC, Poser I, Cox J, Nagaraj N, Toyoda Y, Gak IA, Weisswange I, Mansfeld J, Buchholz F *et al* (2015) A human interactome in three quantitative dimensions organized by stoichiometries and abundances. *Cell* 163: 712 – 723

Hirano Y, Yoshinaga S, Takeya R, Suzuki NN, Horiuchi M, Kohjima M, Sumimoto H, Inagaki F (2005) Structure of a cell polarity regulator, a complex between atypical PKC and Par6 PB1 domains. *J Biol Chem* 280: 9653 – 9661

Ishihara N, Hamasaki M, Yokota S, Suzuki K, Kamada Y, Kihara A, Yoshimori T, Noda T, Ohsumi Y (2001) Autophagosome requires specific early Sec proteins for its formation and NSF/SNARE for vacuolar fusion. *Mol Biol Cell* 12: 3690 – 3702

Ishiura H, Sako W, Yoshida M, Kawarai T, Tanabe O, Goto J, Takahashi Y, Date H, Mitsui J, Ahsan B *et al* (2012) The TRK-fused gene is mutated in hereditary motor and sensory neuropathy with proximal dominant involvement. *Am J Hum Genet* 91: 320 – 329

Itakura E, Mizushima N (2010) Characterization of autophagosome formation site by a hierarchical analysis of mammalian Atg proteins. *Autophagy* 6: 764 – 776

Jacomin AC, Samavedam S, Promponas V, Nezis IP (2016) iLIR database: A web resource for LIR motif-containing proteins in eukaryotes. *Autophagy* 12: 1945 – 1953

Jeong YT, Simoneschi D, Keegan S, Melville D, Adler NS, Saraf A, Florens WMP, Cavasotto CN, Fenyö D, Cuervo AM *et al* (2018) The ULK1-FBXW5-SEC23B nexus controls autophagy. *eLife* 7: e42253

Johansen T, Lamark T (2020) Selective autophagy: ATG8 family proteins, LIR motifs and cargo receptors. *J Mol Biol* 432: 80 – 103

Johnson A, Bhattacharya N, Hanna M, Pennington JG, Schuh AL, Wang L, Otegui MS, Stagg SM, Audhya A (2015) TFG clusters COPII-coated transport carriers and promotes early secretory pathway organization. *EMBO J* 34: 811 – 827

Karanasios E, Stapleton E, Manifava M, Kaizuka T, Mizushima N, Walker SA, Ktistakis NT (2013) Dynamic association of the ULK1 complex with omegasomes during autophagy induction. *J Cell Sci* 126: 5224 – 5238

Karanasios E, Walker SA, Okkenhaug H, Manifava M, Hummel E, Zimmermann H, Ahmed Q, Domart M-C, Collinson L, Ktistakis NT (2016) Autophagy initiation by ULK complex assembly on ER tubulovesicular regions marked by ATG9 vesicles. *Nat Commun* 7: 12420

Kirkham MB (1974) Trace elements in sludge. *Science* 184: 1030

Kraft C, Kijanska M, Kalie E, Siergiejuk E, Lee SS, Semplicio G, Stoffel I, Brezovich A, Verma M, Hansmann I *et al* (2012) Binding of the Atg1/ULK1 kinase to the ubiquitin-like protein Atg8 regulates autophagy. *EMBO J.* 31: 3691 – 3703

Liu C-C, Lin Y-C, Chen Y-H, Chen C-M, Pang L-Y, Chen H-A, Wu P-R, Lin M-Y, Jiang S-T, Tsai T-F *et al* (2016) Cul3-KLHL20 ubiquitin ligase governs the turnover of ULK1 and VPS34 complexes to control autophagy termination. *Mol Cell* 61: 84 – 97

Liu X, Li Y, Wang X, Xing R, Liu K, Gan Q, Tang C, Gao Z, Jian Y, Luo S *et al* (2017) The BEACH-containing protein WDR81 coordinates p62 and LC3C to promote aggrephagy. *J Cell Biol* 216: 1301 – 1320

Lord C, Bhandari D, Menon S, Ghassemian M, Nycz D, Hay J, Ghosh P, Ferro-Novick S (2011) Sequential interactions with Sec23 control the direction of vesicle traffic. *Nature* 473: 181 – 186

Mizushima N, Kuma A, Kobayashi Y, Yamamoto A, Matsubae M, Takao T, Natsume T, Ohsumi Y, Yoshimori T (2003) Mouse Apg16L, a novel WD-repeat protein, targets to the autophagic isolation membrane with the Apg12-Apg5 conjugate. *J Cell Sci* 116: 1679 – 1688

Mizushima N, Yoshimori T, Ohsumi Y (2011) The role of Atg proteins in autophagosome formation. *Annu Rev Cell Dev Biol* 27: 107 – 132

Moyer BD, Allan BB, Balch WE (2001) Rab1 interaction with a GM130 effector complex regulates COPII vesicle cis–Golgi tethering. *Traffic* 2: 268 – 276

von Muhlinen N, Akutsu M, Ravenhill BJ, Foeglein Á, Bloor S, Rutherford TJ, Freund SMV, Komander D, Randow F (2012) LC3C, bound selectively by a noncanonical LIR motif in NDP52, is required for antibacterial autophagy. *Mol Cell* 48: 329 – 342

Nazio F, Carinci M, Valacca C, Bielli P, Strappazzon F, Antonioli M, Ciccosanti F, Rodolfo C, Campello S, Fimia GM *et al* (2016) Fine-tuning of ULK1 mRNA and protein levels is required for autophagy oscillation. *J Cell Biol* 215: 841 – 856

Nishimura T, Kaizuka T, Cadwell K, Sahani MH, Saitoh T, Akira S, Virgin HW, Mizushima N (2013) FIP200 regulates targeting of Atg16L1 to the isolation membrane. *EMBO Rep* 14: 284 – 291

Nishimura T, Tamura N, Kono N, Shimanaka Y, Arai H, Yamamoto H, Mizushima N (2017) Autophagosome formation is initiated at phosphatidylinositol synthase-enriched ER subdomains. *EMBO J* 36: 1719 – 1735

Piovesan D, Tabaro F, Paladin L, Necci M, Micetic I, Camilloni C, Davey N, Dosztányi Z, Mészáros B, Monzon AM *et al* (2018) MobiDB 3.0: more annotations for intrinsic disorder, conformational diversity and interactions in proteins. *Nucleic Acids Res* 46: 471 – 476

Piovesan D, Walsh I, Minervini G, Tosatto SCE (2017) FELLS: fast estimator of latent local structure. *Bioinformatics* 33: 1889 – 1891

Quintarelli C, Orlando D, Boffa I, Guercio M, Polito VA, Petretto A, Lavarello C, Sinibaldi M, Weber G, Del Bufalo F *et al* (2018) Choice of costimulatory

© 2021 The Authors

domains and of cytokines determines CAR T-cell activity in neuroblastoma. *Oncoimmunology* 7: e1433518

Rogov V, Dötsch V, Johansen T, Kirkin V (2014) Interactions between autophagy receptors and ubiquitin-like proteins form the molecular basis for selective autophagy. *Mol Cell* 53: 167 – 178

Schlundt A, Sticht J, Piotukh K, Kosslick D, Jahnke N, Keller S, Schuemann M, Krause E, Freund C (2009) Proline-rich Sequence Recognition. *Mol Cell Proteomics* 8: 2474 – 2486

Slobodkin MR, Elazar Z (2013) The Atg8 family: multifunctional ubiquitin-like key regulators of autophagy. *Essays Biochem* 55: 51 – 64

Söding J, Biegert A, Lupas AN (2005) The HHpred interactive server for protein homology detection and structure prediction. *Nucleic Acids Res* 33: 244 – 248

Stadel D, Millarte V, Tillmann KD, Huber J, Tamin-Yecheskel B-C, Akutsu M, Demishtein A, Ben-Zeev B, Anikster Y, Perez F *et al* (2015) TECPR2 cooperates with LC3C to regulate COPII-dependent ER export. *Mol Cell* 60: 89 – 104

Steinmetz TD, Schlötzer-Schrehardt U, Hearne A, Schuh W, Wittner J, Schulz SR, Winkler TH, Jäck H-M, Mielenz D (2020) TFG is required for autophagy flux and to prevent endoplasmic reticulum stress in CH12 B lymphoma cells. *Autophagy* 22: 1 – 19

Takashima H, Nakagawa M, Nakahara K, Suehara M, Matsuzaki T, Higuchi I, Higa H, Arimura K, Iwamasa T, Izumo S *et al* (1997) A new type of hereditary motor and sensory neuropathy linked to chromosome 3. *Ann Neurol* 41: 771 – 780

Tsai P-C, Huang Y-H, Guo Y-C, Wu H-T, Lin K-P, Tsai Y-S, Liao Y-C, Liu Y-T, Liu T-T, Kao L-S *et al* (2014) A novel TFG mutation causes Charcot-Marie-Tooth disease type 2 and impairs TFG function. *Neurology* 83: 903 – 912

Verhoeven K, De Jonghe P, Coen K, Verpoorten N, Auer-Grumbach M, Kwon JM, FitzPatrick D, Schmedding E, De Vriendt E, Jacobs A *et al* (2003) Mutations in the small GTP-ase late endosomal protein RAB7 cause charcot-marie-tooth type 2B neuropathy. *Am J Hum Genet* 72: 722 – 727

Wang J, Tan D, Cai Y, Reinisch KM, Walz T, Ferro-Novick S (2014) A requirement for ER-derived COPII vesicles in phagophore initiation. *Autophagy* 10: 708 – 709

Webb B, Sali A (2017) Protein structure modeling with MODELLER. *Methods Mol Biol.* 1654: 39 – 54

Wetzel L, Blanchard S, Rama S, Beier V, Kaufmann A, Wollert T (2020) TECPR1 promotes aggrephagy by direct recruitment of LC3C autophagosomes to lysosomes. *Nat Commun* 11: 2993

Willard L, Ranjan A, Zhang H, Monzavi H, Boyko RF, Sykes BD, Wishart DS (2003) VADAR: a web server for quantitative evaluation of protein structure quality. *Nucleic Acids Res* 31: 3316 – 3319

Wirth M, Zhang W, Razi M, Nyoni L, Joshi D, O'Reilly N, Johansen T, Tooze SA, Mouilleron S (2019) Molecular determinants regulating selective binding of autophagy adapters and receptors to ATG8 proteins. *Nat Commun* 10: 2055

Witte K, Schuh AL, Hegermann J, Sarkeshik A, Mayers JR, Schwarze K, Yates JR, Eimer S, Audhya A (2011) TFG-1 function in protein secretion and oncogenesis. *Nat Cell Biol* 13: 550 – 558

Zacharias J, Knapp EW (2014) Protein secondary structure classification revisited: processing DSSP information with PSSC. *J Chem Inf Model* 54: 2166 – 2179

Zoppino FCM, Militello RD, Slavin I, Alvarez C, Colombo MI (2010) Autophagosome formation depends on the small GTPase Rab1 and functional ER exit sites. *Traffic* 11: 1246 – 1261

License: This is an open access article under the terms of the Creative Commons Attribution-NonCommercial-NoDerivs License, which permits use and distribution in any medium, provided the original work is properly cited, the use is non-commercial and no modifications or adaptations are made.

 © 2021 The Authors